Journal of
Materials Chemistry B

PAPER

View Article Online
View Journal | View Issue

Check for updates

Cite this: *J. Mater. Chem. B*, 2025, **13**, 13360

Hybrid methacrylated PCL/inulin photosensitive resins for 3D printing: a step forward in bone tissue engineering

Carmela Tommasino,[ab] Carla Sardo,[a] Angiola Guidone,[ab] Maria Grazia Raucci,[c] Anna Mariano,[c] Alessandra Soriente,[c] Rita Patrizia Aquino,[a] Matthew P. Wylie,[d] Giulia Auriemma*[a] and Dimitrios A. Lamprou*[d]

This study addresses the need for innovative, biocompatible photopolymerizable resins for resin-based 3D printing (3DP) in bone tissue engineering (BTE). A new class of hybrid resins was developed by combining polycaprolactone trimethacrylate (PCLTMA) of two molecular weights with methacrylated inulin (INUMA) at varying concentrations. This strategy aimed to overcome the hydrophobicity and slow degradation of PCL by introducing a more hydrophilic and bioactive component, while maintaining high printability. The resins were characterized and processed into macroporous scaffolds *via* stereolithography (SLA). The resulting scaffolds were evaluated for dimensional accuracy, surface topography, mechanical properties, wettability, swelling, and degradation. Biological performance was assessed using human mesenchymal stem cells (hMSCs) and SAOS-2 cells, focusing on cytocompatibility, cell adhesion and osteogenic potential. Results showed that scaffold properties could be tuned by varying PCLTMA molecular weight and INUMA content. Specifically, decreasing PCLTMA molecular weight enhanced crosslinking density and mechanical strength, while increasing INUMA content improved wettability, swelling capacity, and biodegradability. All scaffolds demonstrated good cytocompatibility and supported hMSCs adhesion, confirming suitability for biomedical use. Furthermore, an optimized drug-eluting scaffold incorporating raloxifene hydrochloride (RAL) was developed, achieving uniform drug distribution and a sustained release profile for potential application in localized osteoporosis therapy. This study advances the design of photopolymerizable resins for SLA-based scaffold fabrication. It highlights how the integration of components with different physical and chemical properties can lead to homogeneous hybrid biomaterials that address the limitations of individual components. These findings lay a strong foundation for enhancing resin-based 3DP technologies in BTE and regenerative medicine.

Received 26th May 2025,
Accepted 17th September 2025

DOI: 10.1039/d5tb01262g

rsc.li/materials-b

Introduction

Photopolymerization-based three-dimensional printing (3DP) represents a rapidly advancing branch of additive manufacturing that enables the fabrication of complex, high-resolution structures through photo-induced polymerization of liquid resins. This approach falls within the broader category of vat photopolymerization (VAT), which includes technologies such as stereolithography (SLA), digital light processing (DLP), and UV liquid crystal display (LCD).[1,2] Despite differences in light sources and exposure modalities, these techniques share common advantages such as high resolution (1–10 μm),[3] remarkable design flexibility, and the ability to produce finely structured, micro/macro-porous scaffolds.

Such features make VAT-based 3DP highly attractive for bone tissue engineering (BTE), where architectural precision and porosity directly influence nutrient diffusion, cell migration, and tissue integration.[4,5] Moreover, compared to extrusion-based systems, VAT processes are nozzle-free, operate at room temperature, and are shear-free, enabling the incorporation of thermolabile agents, including bioactive molecules or even cells, into printable formulations.[4,6–8]

Despite these advantages, the broader biomedical implementation of VAT 3DP remains limited due to the scarcity of biocompatible and biodegradable photopolymer resins.[9–11]

---

[a] *Department of Pharmacy, University of Salerno, Via Giovanni Paolo II 132, I-84084 Fisciano (SA), Italy. E-mail: gauriemma@unisa.it*
[b] *PhD Program in Drug Discovery and Development, University of Salerno, Via Giovanni Paolo II 132, I-84084 Fisciano (SA), Italy*
[c] *Institute of Polymers, Composites and Biomaterials, National Research Council of Italy (IPCB-CNR), Viale John Fitzgerald Kennedy 54, Mostra d'Oltremare Padiglione 20, 80125, Naples, Italy*
[d] *School of Pharmacy, Queen's University of Belfast, 97 Lisburn Road, Belfast BT9 7BL, UK. E-mail: d.lamprou@qub.ac.uk*

This creates a critical bottleneck for the development of resin-based scaffolds in regenerative medicine. This study addresses this gap by proposing customizable photopolymer resins with improved biocompatibility and degradability, tailored for resin-based scaffold fabrication.

Poly(ε-caprolactone) (PCL) is one of the most widely studied synthetic polymers in BTE due to its biocompatibility, bioresorbability, ease of processing, and cost-effectiveness.[12] Functionalized forms such as PCL diacrylate, trimethacrylate, or fumarate have been developed to render PCL suitable for photopolymerization.[13–17] Nevertheless, these materials still exhibit key limitations of native PCL, namely hydrophobicity, slow degradation, and limited bioactivity, which constrain their use in advanced regenerative systems.[12,18,19]

To overcome these drawbacks, formulating hybrid photopolymerizable resins by blending PCL derivatives with functional co-monomers or polymers has emerged as a promising strategy. Such combinations allow for the fine-tuning of degradation, mechanics, and biofunctionality without compromising 3DP compatibility. Natural or synthetic additives such as PLA (dimensional control),[20] collagen (bioactivity),[15] or bioceramics (osteoconduction)[19,21,22] have been integrated into photocurable systems to enhance performance.

Among these, the use of additional photocrosslinkable polymers is particularly attractive because they can chemically participate in the network formation.[18,23,24] Gelatin methacrylate (GelMA) is a well-known example, but its limited mechanical strength[25] and potential immunogenicity[26] motivate the search for alternative semi-synthetic options.[25,27]

To address these limitations, this study proposes a hybrid resin strategy that combines polycaprolactone trimethacrylate (PCLTMA) with methacrylated inulin (INUMA), a photocrosslinkable derivative of the natural polysaccharide inulin. Owing to its flexible backbone and high density of modifiable hydroxyl groups, inulin serves as an excellent platform for chemical functionalization, enabling tailored physicochemical properties and crosslinking behavior.[28–31] Beyond its structural versatility, inulin and its derivatives have shown promising effects on bone health, including enhancement of cortical bone mineral content, regulation of bone remodelling homeostasis, and suppression of bone resorption.[32–34] Notably, some inulin derivatives have also been reported to stimulate osteoblast proliferation, differentiation, and mineralization *in vitro*, suggesting potential for direct biological contributions in BTE contexts.[35] While methacrylated inulin have been previously explored in hydrogel-based drug delivery systems,[36,37] it has never been investigated as a component of hybrid SLA-printable resins for bone scaffold fabrication. In this study, INUMA is expected to contribute not only to the hydrophilicity and degradability of the scaffold, but also to its biological performance, providing an integrated chemical and biofunctional approach for resin formulation in bone tissue engineering.

This study aims to (i) develop and characterize a new class of photopolymerizable hybrid resins based on PCLTMA and INUMA; (ii) investigate how the molecular weight of PCLTMA and the INUMA concentration affect scaffold performance; and (iii) identify the optimal composition for further functionalization with raloxifene hydrochloride (RAL), a clinically used anti-osteoporotic drug.

By systematically investigating the structure–property–function relationships of these hybrid scaffolds, including printability, mechanical strength, degradation behaviour, and cytocompatibility with human mesenchymal stem cells, this work addresses a critical gap in the literature and sets the stage for future applications of hybrid photopolymerizable resins in personalized bone regeneration and regenerative medicine.

Materials and methods

Materials

The three polymeric precursors and the reagents for methacrylates synthesis were supplied as described below:

– Polycaprolactone Triol Mn 500 Da ($PCLT_{500}$) was from Biosynth (Compton, United Kingdom),

– Polycaprolactone Triol Mn 300 Da ($PCLT_{300}$), inulin from Dahlia tubers Mn ~5000 Da (INU), methacrylic anhydride (≥98%, containing 2000 ppm topanol A as inhibitor) (MA), triethylamine for synthesis (≥99%) (TEA), anhydrous *N*,*N*-dimethyl formamide (≥99.75%) (a-DMF), dichloromethane (analytical grade) (DCM) (2,4,6-trimethylbenzoyl)diphenylphosphine oxide (>96.5%) (TPO) and β-carotene (synthetic, ≥95%, crystalline), deuterated chloroform ($CDCl_3$), deuterium oxide (D_2O), dimethyl sulfoxide (ACS reagent grade, ≥99.9%) (DMSO), sodium azide (for synthesis, >99.0%) (NaN_3) were from Merck (Darmstadt, Germany).

– Raloxifene hydrochloride (>98%) (RAL) was supplied from Prodotti Gianni S.r.l. (Milan, Italy).

– DCM was dried over activated molecular sieves (4 Å) before its use.

– All other chemical reagents and solvents were used as received.

Synthesis of photopolymerizable resin components

Synthesis of PCLTMA. PCLTMA was synthesized with two different molecular weights, 300 Da (lower molecular weight) and 500 Da (higher molecular weight), referred to as $PCLTMA_{300}$ and $PCLTMA_{500}$, following a protocol reported by Field *et al.*[13] with slight modification. Specifically, $PCLT_{300}$ or $PCLT_{500}$ were reacted with methacrylic anhydride in the presence of an equimolar amount of triethylamine to produce photopolymerizable PCLTMA. The reaction scheme is depicted in Fig. 1.

PCLT (4 g–13.3 mmol for $PCLT_{300}$ or 8.0 mmol for $PCLT_{500}$) was dissolved in 40 mL of anhydrous DCM (a-DCM) and added with TEA (11.15 mL–80.0 mmol for $PCLT_{300}$ or 6.69 mL–48.0 mmol for $PCLT_{500}$). The solution was cooled to 0 °C and purged with nitrogen for 30 minutes. Methacrylic anhydride (11.92 mL–80.0 mmol for $PCLT_{300}$ or 7.15 mL–48.0 mmol for $PCLT_{500}$) was then added dropwise. The reaction mixture was allowed to gradually warm to room temperature and stirred for 24 h. The quantities of reagents were determined according to

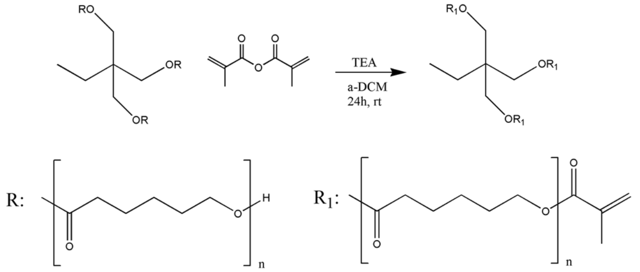

Fig. 1 PCLTMA synthesis reaction scheme.

eqn (1) and (2) molar ratio calculations.

$$R1 = \frac{n_{\mathrm{MA}}}{n_{\mathrm{PCLT}}} = 6 \quad (1)$$

$$R2 = \frac{n_{\mathrm{TEA}}}{n_{\mathrm{MA}}} = 1 \quad (2)$$

where n_{PCLT}, n_{MA}, and n_{TEA} represent the moles of PCL triol, methacrylic anhydride, and triethylamine, respectively.

After 24 hours, DCM was removed by rotary evaporation, and the oily residue was washed four times with double-distilled water to remove unreacted MA. The resulting product, a yellowish liquid, was stored at −20 °C until further use. All syntheses were performed at least in triplicate to ensure reproducibility.

Synthesis of INUMA. INUMA was synthesized following the method reported by Tripodo *et al.*[36] Prior to use, INU was dried for 24 h at 70 °C in a static oven. Subsequently, 1 g (6.2 mmol of fructose repeating units) of the dried INU was dissolved in 14 mL of a-DMF under a nitrogen atmosphere. After complete dissolution, appropriate amounts of TEA (215 μL–1.5 mmol) as a catalyst and MA (460 μL–3.1 mmol) were added (Fig. 2), maintaining a molar ratio of (calculated using eqn (3) and (4)):

$$R1 = \frac{n_{\mathrm{MA}}}{n_{\mathrm{RUINU}}} = 0.5 \quad (3)$$

$$R1 = \frac{n_{\mathrm{TEA}}}{n_{\mathrm{MA}}} = 0.5 \quad (4)$$

where n_{RUINU}, n_{MA}, and n_{TEA} represent the moles of inulin repeating units, methacrylic anhydride, and triethylamine, respectively.

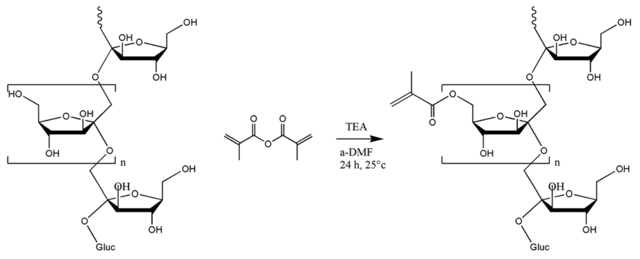

Fig. 2 INUMA synthesis reaction scheme.

The reaction mixture was stirred at 25 °C under nitrogen for 24 h. Upon completion, the product was precipitated in 150 mL of a diethyl ether/acetone mixture (2 : 1 v/v) and isolated by centrifugation for 15 min at 6000 rpm (ALC PK120 centrifuge, Winchester, UK). The solid was washed three times with the same solvent mixture and then dried under reduced pressure. To prevent premature crosslinking, the entire synthesis was conducted in the dark. The final product, a white solid, was stored at room temperature under an inert gas and protected from light until further use. The synthetic procedure was conducted at least in triplicate.

NMR analysis. To characterize the synthetized polymers and determine their molar degree of derivatization (DDmol%), ^{1}H-NMR spectra were recorded using a Bruker Avance III spectrometer (Bruker UK Ltd, Coventry, UK) operating at 400 MHz. $CDCl_3$ and D_2O, were used as solvents for PCLTMA and INUMA, respectively. Samples were prepared by dissolving 10 mg of the polymer in 0.6 mL of the appropriate deuterated solvent. Spectra analysis was performed using Mnova software (Mestrelab).

Resin formulation and preparation. Various blank resin formulations were prepared using the two PCLTMA variants with lower (Resin_PCL$_{300}$) and higher (Resin_PCL$_{500}$) molecular weights. Blends of PCLTMA and INUMA were also formulated at weight ratios of at 90 : 10 (Resin_PCL$_{300}$/Inu10 and Resin_PCL$_{500}$/Inu10) and 80 : 20 (Resin_PCL$_{300}$/Inu20 and Resin_PCL$_{500}$/Inu20). Each formulation included 2.0% w/w of the photoinitiator TPO and 0.1% w/w of the photoabsorber β-carotene. For the preparation of blank resins, INUMA was mixed with PCLTMA and stirred overnight in the dark to ensure homogeneous dispersion. TPO and β-carotene were added to the blend immediately before printing and mixed vigorously using a vortex mixer to ensure complete dissolution. Additionally, a drug-loaded resin, containing PCLTMA$_{300}$ and INUMA in an 80 : 20 ratio, loaded with 1% w/w RAL, was prepared and designated as Resin_PCL$_{300}$/Inu20/RAL. In this formulation, RAL was first dissolved in PCLTMA, followed by the sequential addition of INUMA, TPO, and β-carotene, as described for the blank resins. For detailed resin compositions, refer to Table 1 in the Results and Discussion section.

Table 1 Composition of the photopolymerizable resins used for 3D printing. Resins were formulated by combining PCLTMA (300 or 500 Da) and INUMA at different weight ratios. All formulations included 2.0% w/w TPO and 0.1% w/w β-carotene

Name	PCLTMA$_{300}$ (w/w%)	PCLTMA$_{500}$ (w/w%)	INUMA (w/w%)	TPO (w/w%)	β-carotene (w/w%)
Resin_PCL$_{300}$	97.9	—	—	2.0	0.1
Resin_PCL$_{300}$/Inu10	88.1	—	9.8		
Resin_PCL$_{300}$/Inu20	78.3	—	19.6		
Resin_PCL$_{500}$	—	97.9	—		
Resin_PCL$_{500}$/Inu10	—	88.1	9.8		
Resin_PCL$_{500}$/Inu20	—	78.3	19.6		

Rheological characterization. The viscosity of the resin formulations was evaluated using a HAAKE™ MARS™ Rheometer (Thermo Scientific™, UK) equipped with a parallel plate geometry. Both the upper and lower plates had a diameter of 35 mm, and the gap between them was set to 100 μm. Shear rate was varied from 0.1 to 100 s^{-1} to generate flow curves. The experiments were conducted at 20 °C, and each sample was tested in triplicate to ensure reproducibility.[38] This method allows for the assessment of the flow behaviour of the resins under different shear rates, providing insights into their suitability for various processing conditions.

Optical characterization. Depth of cure experiments were performed to evaluate the penetration depth (D_p) and the critical exposure dose (E_c) of the resin formulations, following the procedure reported by Ahmad *et al.*[39] with slight modifications. Liquid resins were poured into cylindrical polyurethane molds (12.5 mm diameter and 4 mm height), placed on a glass slide, and covered with a Mylar strip. The samples were then irradiated at 405 nm using a 6 W UV lamp for predetermined exposure times (30, 60, 90, 120, and 240 s). After each exposure, the cured resin was extracted and uncured material removed by scraping with a stainless-steel spatula. The final cure depth (Cd) was measured with a digital caliper. The relationship between cure depth and exposure time was then analyzed to construct working curves (logarithmic plots of cure depth *vs.* exposure energy). A linear regression fit was applied to the data in the linear region of the curve. From the slope of the linear fit, the penetration depth (D_p) was calculated, while the intercept with the *x*-axis allowed the determination of the critical exposure dose (E_c).

Fabrication of scaffolds by 3D printing. Rhinoceros 5 Computer-Aided Design (CAD) software (Robert McNeel & Associates, McNeel Europe) was employed for the development of scaffold digital model. A woodpile structure with dimensions of 8.58 (length) × 8.61 (width) × 2.50 mm (height), a pore size of 1.0 mm, and a fiber width of 0.8 mm was designed, exported as stereolithographic (.stl) file to Formlabs' Preform software (version 3.18) for slicing and printing preparation.

3D printing process was performed using a Formlabs Form 2 desktop SLA 3D printer (Somerville, Massachusetts, USA). Printing was conducted in "open mode" to prevent automatic resin tank filling, with "ClearV4" as the material setting. Supports were generated to stabilize the scaffold during printing, and 25° tilt angle was applied to optimize print quality. The process was carried out at room temperature with a layer thickness of 25 μm. Scaffolds were sonicated in 2-propanol (IPA) for 10 min to eliminate uncured resin and were air-dried overnight to ensure complete solvent evaporation.[13,40] These post-processing steps are essential to enhance the mechanical properties and biocompatibility of resin-based 3D printed scaffolds. Proper cleaning and curing protocols help remove residual monomers and improve the overall quality of the printed constructs.

FTIR analysis. Fourier-transform infrared spectroscopy (FTIR) analysis was conducted on raw materials, liquid resins, and 3D printed scaffolds using a Nicolet iS50 FTIR spectrometer (Thermo Fisher Scientific, Waltham, Massachusetts, USA) paired with attenuated total reflectance (ATR), in a spectral range of 400–4000 cm^{-1}, with a run of 64 scans and a 4 cm^{-1} resolution. To facilitate comparison between resins and scaffold spectra, signals were normalized respect to the carbonyl (C═O) stretching peak centered at 1715 cm^{-1}.[41]

To assess the extent of methacrylate conversion during the 3D printing process, FTIR spectra of the liquid resins and the corresponding 3D printed scaffolds were compared. The degree of conversion (DC%) was calculated by monitoring the decrease in the absorbance of the characteristic methacrylate band at 815 cm^{-1} ($CH{=}CH_2$ bending), compared to the reference peak at 1150 cm^{-1} (C–O–C stretching), according to the following equation (eqn (5)):[42]

$$\mathrm{DC}\ (\%) = \frac{\left(\frac{\mathrm{Abs}_{815}}{\mathrm{Abs}_{1150}}\right)_{\mathrm{Resin}} - \left(\frac{\mathrm{Abs}_{815}}{\mathrm{Abs}_{1150}}\right)_{\mathrm{Scaffold}}}{\left(\frac{\mathrm{Abs}_{815}}{\mathrm{Abs}_{1150}}\right)_{\mathrm{Resin}}} \times 100 \qquad (5)$$

Although FTIR is a surface-sensitive technique, the layer-by-layer irradiation of SLA minimizes interior unreacted regions; consequently, FTIR-derived DC% values can be reasonably considered representative of the whole scaffold.

Raman spectroscopy. Raman spectra acquisition was performed using an InVia Qontor Raman microscope (Renishaw, Gloucestershire, UK). With a 785 nm laser and a 50× objective lens. Spectra were collected in the 0–3500 cm^{-1} region with a laser power of 10 mW. Photons scattered by each sample were dispersed by a 1200 lines per mm (514/780) grating monochromator and simultaneously collected on a CCD camera. For each measurement, three spectra were acquired with an acquisition time of 10 seconds each. Spectra analysis was performed utilizing the software WiRE 5.6. The crystallinity (X_c) of PCLTMA was determined by analysing the C═O stretching band (1700–1750 cm^{-1}), considered as the superposition of the intensities of the crystalline (I_c) and amorphous (I_a) spectral components, using the following equation (eqn (6)):[43,44]

$$X_c = \frac{I_c}{I_c + I_a} \times 100 \qquad (6)$$

The Raman maps were performed using an alpha300 Apyron microscope (WITec, Ulm, Germany) with a 532 nm laser and a 100× objective lens. Spectra were collected in the 0–3500 cm^{-1} region with a laser power of 10 mW. Photons scattered by each sample were dispersed by a 600 lines per mm grating monochromator and simultaneously collected on a CCD camera. Spectra analysis was performed utilizing the software WiRE 5.6.

Thermogravimetric analysis (TGA). The thermal stability of methacrylate polymers, resins and 3D printed scaffolds was evaluated by TGA using a Thermal Advantage Q50 TGA (TA Instruments, New Castle, Delaware, USA). Samples (n = 3, 10 mg) were examined in open aluminium pan, and the analysis was performed from room temperature to 500 °C, with a heating rate of 20 °C min^{-1} along with a nitrogen flow rate of 50 mL min^{-1}. The percentage of remaining weight was plotted against temperature (°C), and the onset of degradation was determined from the original data using the first derivative.

Scaffold dimensional, morphological and topographical analysis. The dimensions and thickness of the scaffolds were determined using an electronic digital calliper. For each scaffold, three measurements were taken, and at least three scaffolds were measured. The results were expressed as the mean ± standard deviation (SD).

The scaffolds' morphology and 3D architecture were assessed using an optical microscope (Leica Microsystems EZ4W, Wetzlar, Germany). Images of the top, bottom, and lateral views were captured at a 12.5× magnification and scale bar 1 mm. Pore size and fiber width were measured using the instrument's software. Five measurements were taken per scaffold, and at least three scaffolds were analysed, with results expressed as mean ± SD.

Dimensional error (DE%), indicating the relative deviation from the theoretical size, was evaluated using the following equation (eqn (7)):[45]

$$\mathrm{DE}\% = \frac{\text{theoretical size} - \text{experimental size}}{\text{theoretical size}} \times 100 \qquad (7)$$

Surface topography was investigated using Scanning Electron Microscopy (SEM) and Atomic Force Microscopy (AFM). SEM images were acquired using a Hitachi TM3030 microscope (Tokyo, Japan) at magnifications of 500 and 1000×, scale bar 100 and 200 μm, and accelerating voltage 15 kV. Energy dispersive X-ray (EDX) analysis was performed during imaging. AFM measurements were carried out using an alpha300 Apyron microscope (WITec, Ulm, Germany) with a Zeiss EC Epiplan 20×/0.4 objective. The measurements were conducted in AC mode using an AFM arrow cantilever (spring constant 2.8 N m^{-1}, resonance frequency 75 Hz). The AFM scans were performed over a sample area of 20 × 20 $\mu\mathrm{m}^2$ with a resolution of 256 × 256 pixels. The forward scan speed and retrace speed were set to 1 second. The images acquired were processed using the software WITecProject. A surface background subtraction with an order of 5 was performed, and the average roughness (SA) and root mean square roughness (SQ) were determined. Subsequently, the images were further processed to extract additional surface parameters, including skewness (SSK), kurtosis (SKU), developed interfacial area ratio (SDR), root mean square gradient (SDQ), and peak–peak height.

Mechanical properties evaluation. Scaffold mechanical properties were evaluated through uniaxial compression tests, using a TA.XT Plus texture analyzer (Stable Micro Systems, Surrey, UK), equipped with a 30 kg (294 N) load cell. Samples ($n = 3$) were compressed perpendicularly to their larger surface at a crosshead speed of 1.2 mm min^{-1} (with a pre-test speed 60 mm min^{-1} and a post-test speed 600 mm min^{-1}), until 20% strain. Stress–strain curves were obtained from the load *vs.* displacement data using the initial external dimensions of each sample and Young's modulus was calculated using the slope of the linear portion of the stress–strain curve.

Water contact angle measurement. The water contact angle of the scaffolds was measured using a Biolin Theta Tensiometer (Manchester, United Kingdom). 1 μL droplet of deionized water was deposited onto the scaffold surface, and the contact angle was recorded for 10 seconds after the drop placement. The contact angle was calculated using the Young–Laplace equation *via* the Biolin Scientific software One-Attension 1.8. The values are reported as the mean ± SD. All experiments were performed in triplicate.

Swelling behaviour analysis. The swelling ability of the 3D printed scaffolds was evaluated by monitoring the fluid uptake percentage over time in phosphate-buffered saline (PBS) at 37 °C. The scaffolds were accurately weighed (W_0), immersed in 0.1 M PBS (pH 7.4) containing 0.05% w/v $\mathrm{NaN_3}$ to prevent microbial growth.[46] Samples were incubated at 37 °C and retrieved at various time points (1, 2, 3, 7, 14, and 21 days). After removed from the medium, scaffolds were blotted dry to remove excess medium, and their wet weight (W_t) was recorded. The fluid uptake (%) was calculated using the following equation (eqn (8)):

$$\text{Fluid uptake}\,(\%) = \frac{W_t - W_0}{W_0} \times 100 \qquad (8)$$

All measurements were conducted in biological triplicate ($n = 3$ per condition).

***In vitro* degradation studies.** The *in vitro* degradation of the scaffolds was assessed under two different conditions: (1) in 0.1 M PBS (pH 7.4) containing 0.05% w/v $\mathrm{NaN_3}$ to prevent microbial growth, and (2) under accelerated degradation condition using a 1 M NaOH solution. Each scaffold was precisely weighted, placed in individual screw-capped vials containing 10 mL of the selected medium, and incubated at 37 °C. Samples were collected at predetermined time points over a total period of 6 weeks (PBS) or 2 weeks (NaOH). After removal from the medium, scaffolds were thoroughly rinsed with deionized water and dried in an oven at 37 °C for 24 h. The dried samples were weighed at room temperature (20 °C) before being discarded. All experiments were performed in technical triplicate ($n = 3$ per condition).

Drug loading and efficiency evaluation. The drug loading in both the drug-loaded resins and the 3D printed scaffolds (Resin/Scaffold_$\mathrm{PCL_{300}}$/Inu20/RAL) was determined as follows. A 100 mg sample of the resin was diluted in 10 mL of DMSO and thoroughly mixed. For scaffolds analysis, the samples were crushed using a mortar and pestle, and 100 mg of the resulting powder was transferred into a vial containing 10 mL of DMSO. The solutions were then sonicated for 4 hours to ensure complete drug extraction. The same procedure was performed for blank resin and scaffold samples (Resin/Scaffold_$\mathrm{PCL_{300}}$/Inu20) as controls. Subsequently, the solutions were appropriately diluted, and their absorbance was measured at 295 nm using a Genesys 150 UV-vis Spectrophotometer (Thermo Fisher Scientific, Waltham, MA). The drug loading percentage was calculated by subtracting the absorbance of the blank solutions from that of the drug-loaded samples. The RAL concentration was determined using a previously validated RAL calibration curve in DMSO ($y = 0.0549x - 0.0016$, $R^2 = 0.9995$, concentration range: 0.39–15.50 μg mL^{-1}). The loading efficiency was calculated as the percentage ratio between the experimentally determined drug content and the theoretical content (1% w/w). The analysis was conducted in triplicate.

Drug release study. The drug release profile from Scaffold_PCL_{300}/Inu20/RAL was monitored over a period of 10 weeks, in triplicate. Each scaffold (n = 3), containing approximately 1 mg of RAL, was individually placed in a screw-capped vial containing 25 mL of 0.1 M PBS (pH 7.4) supplemented with 0.1% w/v Tween® 80, under sink conditions. The vials were incubated in an Orbital shaker (SKI 4, Argolab, Italy) set at 37 °C and 110 rpm. At predetermined time points, 1 mL aliquots were withdrawn and replaced with an equal volume of fresh medium to maintain sink conditions. The RAL content in the collected aliquots was analysed at 289 nm using a Genesys 150 UV-vis Spectrophotometer (Thermo Fisher Scientific, Waltham, MA), using a validated RAL calibration curve ($y = 0.0375x - 0.0165$, $R^2 = 0.9976$, concentration range: 0.38–37.75 μg mL^{-1}).

The cumulative RAL release data were fitted to six standard kinetic models: first-order, second-order, Hixson–Crowell, Higuchi, Korsmeyer–Peppas, and Weibull. Curve fitting was performed using non-linear regression,[47] and the best-fitting model was identified based on the coefficient of determination (R^2). Model-specific parameters (*e.g.*, n for Korsmeyer–Peppas, b for Weibull) were extracted to infer the release mechanism.

Indirect cytotoxicity assay. Human mesenchymal stem cells at passage 8 (hMSCs-P8) were cultured in Dulbecco's Modified Eagle's Medium (DMEM) high glucose (Sigma-Aldrich, Milan, Italy) supplemented with 10% fetal bovine serum (FBS), an antibiotic solution (streptomycin 100 μg mL^{-1} and penicillin 100 U mL^{-1}), and 2 mM L-glutamine. Cells were maintained in a humidified atmosphere with 5% CO_2 at 37 °C. 10 000 cells per well were seeded into a 96-well plate. After reaching 80% confluency in 3 days, the culture medium was replaced with eluates from scaffolds. Blank scaffolds were incubated with DMEM high glucose at 37 °C for 24 hours. The eluates were then collected and incubated with hMSCs-P8 for 24 hours. Cells cultured in fresh DMEM high glucose without eluates were used as the negative control. Each condition was tested in technical triplicate (n = 3). After an additional 24 hours, cell viability was assessed using an Alamar Blue assay. Alamar Blue solution (10 v/v%) was added to each well and incubated at 37 °C for 3 hours to allow for resazurin to resorufin conversion by cells. The optical density was measured using a UV-vis spectrophotometer (Victor X3 Multilabel Plate Reader, Perkin-Elmer, Waltham, Massachusetts, USA) at wavelengths of 570 and 600 nm.

Scaffold sterilization, cell seeding, adhesion and proliferation assay. To ensure a sterile environment for cell culture, the scaffolds were subjected to a sterilization protocol. Blank scaffolds were individually placed within a 24-well plate and initially immersed in 70% ethanol for 1 hour at room temperature to denature cellular proteins and lipids. Subsequently, they were rinsed twice with sterile distilled water and twice with 1X PBS sterile to remove any residual ethanol. To further reduce microbial contamination, scaffolds were immersed in a 10% penicillin–streptomycin solution for 1 hour at room temperature and finally rinsed three times with sterile 1X PBS to remove any residual antibiotic solution. Drug-loaded scaffolds (Scaffold_PCL_{300}/Inu20/RAL) underwent a modified sterilization protocol. To ensure thorough antimicrobial treatment without compromising drug stability, these scaffolds were immersed in a 10% penicillin–streptomycin solution for 2 hours and subsequently washed three times with sterile 1X PBS. Following sterilization, to equilibrate the pH to physiological values, all scaffolds were placed in 2 mL of Stem Cell Expansion medium (Sigma Aldrich, St. Louis MO, USA) for 1 hour. The plate was then transferred to an incubator at 37 °C. hMSCs at passage 4 (hMSCs-P4), cultured in Stem Cell Expansion medium, were seeded at a density of 8×10^4 cells per well. Specifically, 100 μL of the cell suspension were carefully pipetted dropwise onto each scaffold. The plate was then incubated for 1 hour to allow the cells to attach to the scaffold. After this initial incubation, 2 mL of fresh medium was added to each well, and the plate was placed in a standard incubator at 37 °C with 5% CO_2. The culture medium was changed every 3 days. Each condition was tested in technical triplicate (n = 3). To assess cell viability over time, the AlamarBlue assay was performed at days 1, 3, 7, 14, and 21. After 21 days of cell culture, the cellularized scaffolds were fixed with 10% formalin for 2 hours at 4 °C. The scaffolds were then washed twice with 1X PBS to remove excess fixative. Subsequently, the scaffolds were treated with aqueous ethanol solutions at 25%, 50%, and 75% for 5 minutes each, followed by treatment with 100% ethanol for 10 minutes to dehydrate them. After dehydration, the scaffolds were mounted onto aluminium stubs coated with a gold-palladium alloy and analysed using scanning electron microscopy with a FEI Quanta 200 FEG (Thermo Fisher Scientific, Eindhoven, Netherlands).

Morphological and protein expression analysis by immunofluorescence. SAOS-2 cells were cultured in 48-well plates and maintained for either 7 or 14 days, depending on the experimental time point. At each endpoint, immunofluorescence staining was performed to assess both cell morphology and osteogenic marker expression. Cells were fixed with 10% paraformaldehyde for 1 hour at room temperature (RT), then washed three times with PBS. Permeabilization was achieved using 0.1% Triton X-100 in PBS for 5 minutes at RT, followed by additional PBS washes. To prevent non-specific antibody binding, samples were incubated for 1 hour in a blocking solution containing 2% bovine serum albumin (BSA) in PBS. Cells were then incubated overnight at 4 °C with rabbit polyclonal primary antibodies diluted in blocking buffer: anti-osteocalcin (OCN, Merck; 1 : 200) and anti-collagen type I (Coll I, Proteintech; 1 : 200). After washing, cells were incubated for 1 hour at RT in the dark with the corresponding fluorophore-conjugated secondary antibody (Goat anti-Rabbit IgG H&L, DyLight 488; 1 : 500). Cell membranes were stained with CellMask™ (Thermo Fisher Scientific; 1 : 1000) for 30 minutes at RT in the dark, followed by PBS washes. Nuclei were counterstained with DAPI (1 : 200) for 20 minutes at RT. After final washes, the 48-well plates were mounted on a Leica DMi8 fluorescence microscope and stored at 4 °C in the dark until imaging. Fluorescence images were acquired using appropriate filter sets and a HC PL FLUOTAR 20×/0.40 CORR PH1 objective. Fluorescence images obtained at 7 days (Fig. 14a and b) and 14 days (Fig S23) were processed using Fiji/ImageJ software. Corrected total cell fluorescence (CTCF) was calculated to quantify the intensity of collagen I and osteocalcin signals at 7 days (Fig. 14c), using the formula (eqn (9)):

$$\text{CTCF} = \text{Integrated density} - (\text{area of selected cell} \times \text{mean fluorescence of background readings}) \quad (9)$$

This quantification enabled a reliable comparison of osteogenic marker expression levels between different experimental groups.

In parallel, morphological analysis of cell spreading was performed at day 7 (Fig. 15) using CellMask-stained images. Using Fiji/ImageJ, individual cell areas and perimeter were measured to evaluate differences in cell spreading behaviour under various conditions. This analysis provided additional insight into the influence of scaffold-derived eluates on SAOS-2 cell adhesion and morphology over time.

Statistical analysis. The results are expressed as mean ± SD. Due to the limited availability of in-house synthesized resins and the high material and time demand of scaffold fabrication and characterization, all quantitative analyses were performed on $n = 3$ samples. To accommodate the small sample size, non-parametric statistical tests were selected accordingly: Mann–Whitney U or Kruskal–Wallis followed by Dunn's *post hoc* test for multiple comparisons. Statistically significant differences were denoted as * for $p \leq 0.05$, ** for $p \leq 0.01$, *** for $p \leq 0.001$, **** for $p \leq 0.0001$.

Results and discussion

Synthesis and characterization of photopolymerizable polymers

All precursor polymers (PCLT_{300}, PCLT_{500}, and INU) were functionalized with methacrylate groups using methacrylic anhydride and triethylamine as proton scavenger. This process yielded methacrylated derivatives, referred to as PCLTMA_{300}, PCLTMA_{500}, and INUMA, respectively. The precursors and their corresponding methacrylated products were characterized *via* ^{1}H-NMR spectroscopy to confirm the reaction and determine the DDmol%, defined as the percentage of hydroxyl groups that have been functionalized with methacrylate moieties.

For PCLTMA, methacrylation was confirmed by the appearance of peaks at 6.09 ppm (i), 5.55 ppm (j), 1.93 ppm (k), and 4.14 ppm (a″). Moreover, the reduction in intensity of the peak at 3.64 ppm (a′), corresponding to hydroxyl (–OH) groups in the original PCL triol, indicated their substitution by methacrylate moieties[13] (Fig. S1).

DDmol% was determined by comparing the integral of methacrylate proton peaks representing at 6.09 ppm and 5.55 ppm (i, j) with the integral of the methyl group peak at 0.88 ppm (h).[13,48] The DDmol% was 82.65 ± 9.88% for PCLTMA_{300} and 61.25 ± 3.45% for PCLTMA_{500}.

Similarly, successful inulin methacrylation was confirmed by the appearance of peaks at 6.09, 5.55 and 1.93 ppm (h, g, i), characteristic of methacrylate groups (Fig. S2). DDmol% was calculated by comparing the integrals of peaks of methacrylate protons at 6.09 ppm and 5.55 ppm, with the integral of peaks between 3.50 and 4.25 ppm (corresponding to 7 protons from the INU repeating unit),[36] yielding a result of 24.60 ± 4.93%.

Formulation and characterization of photopolymerizable resins

Resin formulation. Six different drug-free (blank) resins were developed for 3DP *via* SLA technology. These formulations incorporated different combinations of PCLTMA with varying molecular weights, either alone or blended with INUMA at weight ratios of 90 : 10 or 80 : 20, as detailed in Table 1. For photopolymerization 3DP, an essential requirement is the material's ability to rapidly polymerize upon light exposure, ideally within seconds.[49] To achieve this, two key additives were incorporated: (1) a photoinitiator, that generates radicals upon UV irradiation, initiating polymerization, and (2) a photoabsorber, that regulates light penetration into the resin, preventing irradiation beyond the designated layer height and facilitating the creation of intricate structures with high resolution.[50]

Among commercially available photoinitiators, TPO was selected as it is the most widely used photoinitiator in polycaprolactone acrylate/methacrylate-based resins.[20,51–53] TPO exhibits a maximum absorption at 380.5 nm,[54] which closely matches the 405 nm wavelength emitted by the 3D printer used in this study. Additionally, β-carotene was identified as a biocompatible photoabsorber for the resin formulation. This natural pigment, extracted from plants and fruits, is FDA approved for use as a nutrient and as a colour additive in drugs and cosmetics and possesses strong antioxidant properties, making it an ideal candidate for biomedical applications.[55]

β-Carotene has been previously studied as a component in PCL-based functionalized resins.[13] Specifically, β-carotene has a broad absorption spectrum, including significant absorption peaks at 449, 478, and 518 nm, as well as strong absorption at 405 nm,[13] the wavelength utilized by the selected printer.

Preliminary experiments were conducted to optimize the concentration of these additives. TPO was tested at concentrations ranging from 0.5 to 4% w/w. β-Carotene was tested at concentrations between 0.05 and 0.3% w/w. Results indicated that low or absent photoabsorber concentrations led to excessive light penetration and over-curing, causing fiber fusion within the construct. Excessive β-carotene concentrations caused under-curing, leading to structural thinning and fragility. Thus, the optimal concentrations were determined to be: 2% w/w TPO and 0.1% w/w β-Carotene. These concentrations ensured adequate crosslinking and improved structural integrity.

Resin characterization. All formulated resins were characterized to evaluate their key physicochemical properties, including viscosity (*via* rheological analysis), chemical composition (*via* FTIR spectroscopy), thermal stability (*via* TGA), and optical parameters relevant to photopolymerization efficiency.

Viscosity is a critical parameter for determining the printability of a resin for 3DP. The optimal viscosity range for resin-based 3DP has been reported to be 0.01–5 Pa s.[56] The significance of viscosity lies in its influence on monomer mobility.

Lower resin viscosity enhances monomer diffusion, facilitating interactions between reactive groups and accelerating polymerization.[50] Additionally, in bottom-up resin 3D printers, such as the one used in this study, viscosity influences adhesion to the build plate. As the material at the vat bottom solidifies and the platform lifts, viscous forces assist in part separation from the build plate. Therefore, maintaining low resin viscosity is essential. Highly viscous resins may require organic solvents as diluents, which can lead to shrinkage in the final construct,[57] negatively impact mechanical properties,[58] introduce potential cytotoxicity, and raise environmental concerns in the context of large-scale production.[58]

To evaluate the printability of the developed resins for the SLA 3DP, viscosity was analysed using a rotational shear ramp test. All resins exhibited low viscosity (Fig. S3), confirming their suitability for SLA printing without the need for additional diluents.

– PCLTMA-based resins (irrespective of molecular weight) exhibited a viscosity of 0.020 Pa s at a shear rate of $\sim$10 s^{-1}.

– Resins containing INUMA (in a PCLTMA : INUMA ratio of 90 : 10) showed viscosity values comparable to PCLTMA alone.

– Higher INUMA content (PCLTMA : INUMA ratio of 80 : 20) led to increased viscosity, reaching approximately 0.060 Pa s for Resin_PCL$_{300}$/Inu20 and 0.117 Pa s for Resin_PCL$_{500}$/Inu20.

To confirm the chemical composition of the resins and the presence of methacrylate groups essential for polymerization, FTIR analysis was conducted. The obtained spectra were compared with those of the raw materials (Fig. S4 and S5 and Table S1). Key peaks identified included:

– $-CH_3$ stretching: 2850–2950 cm^{-1}

– C–O–C stretching: 1150 cm^{-1} and 1017 cm^{-1}

– –OH stretching (INUMA): 3000–3500 cm^{-1}

– C=O stretching (PCLTMA): 1715 cm^{-1}

– Methacrylate C=C stretching and bending: 1635 cm^{-1} and 815 cm^{-1}, respectively.

The presence of these peaks confirmed successful methacrylation and resin composition.

Thermal stability of the hybrid resins was assessed *via* TGA to investigate their decomposition behaviour at elevated temperatures and explore their potential for applications beyond standard SLA printing conditions. While these materials exhibit inherently low viscosity, ensuring optimal printability at ambient temperature, thermal characterization provides key insights into their structural stability. This information is particularly relevant for potential adaptations in high-temperature environments where tailored processing conditions might further enhance material properties.

The methacrylate polymers and formulated resins exhibited distinct thermal degradation stages. PCLTMA degradation (Fig. S6a and b) proceeded through three main stages: the initial elimination of volatile methacrylate groups at 140 °C, consistent with literature reports;[59] subsequent backbone decomposition at 300 °C, and complete degradation at 480 °C. INUMA (Fig. S6c) exhibited a two-step degradation pattern, with the release of volatile groups at 239 °C, followed by further polymer decomposition at 300 °C.

Hybrid resins retained the characteristic thermal decomposition profiles of both components, displaying distinct degradation events. The initial stage (130 °C) corresponds to the elimination of volatile species, followed by the degradation of INUMA at 240 °C. Around 300 °C, an overlapping degradation of both INUMA and PCLTMA was observed, culminating in the final degradation stage of PCLTMA at 476 °C (Fig. S7).

To further evaluate the suitability of the developed resins for SLA printing, their optical properties were investigated. In particular, depth of cure experiments were performed to determine two key parameters: the penetration depth (D_p) which reflects how deeply UV light can effectively penetrate the resin before being significantly absorbed or scattered, and the critical exposure dose (E_c), defined as the minimum energy required to initiate polymerization.

The working curves obtained from UV-cured samples showed a clear linear relationship in the semi-logarithmic plots, enabling calculation of both D_p and E_c for each formulation (Table 2).

Formulations containing methacrylated inulin exhibited reduced D_p values compared to pristine PCLTMA-based resins. For instance, the D_p of Resin_PCL$_{300}$ decreased from 570 μm to 246 μm when 20% INUMA was added (Resin_PCL300/Inu20). This reduction is attributed to UV scattering by inulin domains and reduced light propagation within the matrix.[60] E_c values ranged from 5.99 to 7.36 mJ cm^{-2}, which are in line with those reported for commercial SLA resins.[61]

Importantly, all resins displayed sufficient D_p and acceptable E_c values to ensure efficient layer-by-layer polymerization under SLA conditions.[60,61] These findings confirm the compatibility of the formulations with commercial open-platform SLA printers.

Development and characterization of 3D printed scaffolds

Scaffold fabrication. Once the suitability of the resins for SLA 3DP was confirmed, they were used as starting materials

Table 2 Optical parameters of PCL$_{300}$- and PCL$_{500}$-based resins calculated from the working curve: penetration depth (D_p), reduction in penetration depth compared to the neat PCL resin, and critical exposure dose (E_c)

Name	Penetration depth – D_p (μm)	D_p reduction (%)	Critical exposure dose – E_c (mJ cm^{-2})
Resin_PCL$_{300}$	570.94	—	7.36
Resin_PCL$_{300}$/Inu10	348.06	39.04	6.36
Resin_PCL$_{300}$/Inu20	246.98	56.87	5.99
Resin_PCL$_{500}$	405.44	—	7.18
Resin_PCL$_{500}$/Inu10	347.47	14.30	6.36
Resin_PCL$_{500}$/Inu20	291.58	28.08	5.99

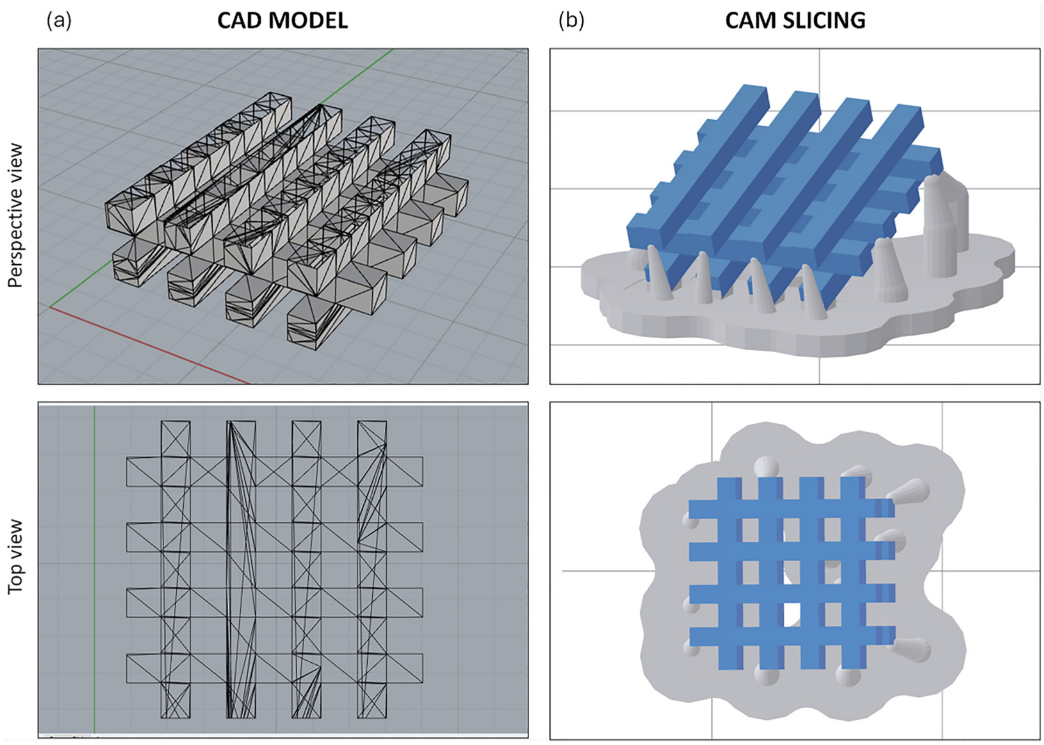

Fig. 3 Scaffold CAD model designed using Rhinoceros 5 (woodpile structure, 8.58 × 8.61 × 2.50 mm) (a) and CAM slicing obtained by Preform 3.18 (support structure, tilt angle 25°, layer thickness 25 μm, 219 layers) (b).

for scaffold fabrication. The first step in obtaining highly reproducible constructs with a precise 3D architecture suitable for bone applications involved designing a digital model using CAD software (Fig. 3a). A woodpile structure was selected due to its resemblance to bone trabeculae.[62] This design provides multiple adhesion sites at the free ends of the fibers, potentially enhancing bone cell attachment, proliferation, and migration within the scaffold.[63]

The digital model was then exported in.stl format, and several preliminary experiments were conducted to optimize the printing parameters. These experiments focused on: printing temperature, layer thickness, positioning of the object on the building platform, printing orientation, and support structure generation. All parameters were fine-tuned using the CAM software provided with the 3D printer (Fig. 3b).

Printing was performed at room temperature, as the resins already exhibited low viscosity, eliminating the need for high-temperature processing. However, preliminary thermal analysis suggested that processing at temperatures up to 130 °C remains a viable option for future applications requiring further viscosity reduction or enhanced crosslinking.

Layer height is a critical parameter in SLA, influencing resin polymerization, printing accuracy, and mechanical properties.[4,64] While thinner layers improve precision and surface smoothness, they also prolong printing time. In this study, a layer height of 25 μm was selected to balance production speed and construct quality.[65] The printing angle also played a crucial role in scaffold integrity and porosity.

Initial tests with angles ranging from 0° to 30° revealed that: a 0° angle led to excessive platform adhesion, making support removal difficult and compromising the porous structure, while steeper angles ($>25°$) resulted in structural collapse during printing. After optimization, a 25° printing angle was identified as the best compromise, ensuring structural integrity and optimal porosity.

The systematic optimization of printing parameters enabled the fabrication of scaffolds with consistent, high-precision architectures across all resin formulations (Fig. S11). All optimized scaffolds exhibited perpendicular fiber arrangements, fiber diameters between 0.918 and 1.000 mm, and square-shaped pores ranging from 0.826 to 0.907 mm (Table 3). To evaluate the discrepancy of the printed scaffolds relative to the CAD model, a dimensional error (DE%) index was calculated (Table 3). Compared to the digital model, the scaffolds demonstrated good dimensional accuracy. A slight increase in fiber width (indicated by negative DE% values) was observed, resulting in a minor reduction in pore size ($DE\% > 0$).

Nevertheless, most DE% values remained below 20%, confirming high agreement ($>80\%$) between the printed scaffolds and the digital design.

Physicochemical characterization. To assess the degree of crosslinking achieved during photopolymerization, FTIR spectra of the 3D printed scaffolds were compared with those of their corresponding liquid resins prior to printing (Fig. S12). This analysis provides valuable insight into the crosslinking extent, a crucial key factor influencing the physicochemical and mechanical properties of the scaffolds.[13]

Table 3 Scaffold dimensional analysis: dimensions, fiber width and pore size, with indication for each of experimental size (n = 3, results expressed as mean ± SD) and dimensional error (DE)

	Scaffold dimensions									
	x		y		z		Fiber width		Pore size	
Name	Exp. size (mm)	DE (%)	Exp. size (mm)	DE (%)	Exp. size (mm)	DE (%)	Exp. size (mm)	DE (%)	Exp.size (mm)	DE (%)
Scaffold_PCL$_{300}$	8.43 ± 0.07	1.70	8.50 ± 0.16	1.32	2.65 ± 0.14	−6.07	0.957 ± 0.022	−19.67	0.877 ± 0.040	12.34
Scaffold_PCL$_{300}$/Inu10	8.47 ± 0.16	1.29	8.56 ± 0.19	0.57	2.69 ± 0.12	−7.40	0.930 ± 0.028	−16.21	0.907 ± 0.061	9.35
Scaffold_PCL$_{300}$/Inu20	8.60 ± 0.08	−0.21	8.58 ± 0.10	0.36	2.62 ± 0.08	−4.71	0.938 ± 0.027	−17.21	0.881 ± 0.037	11.89
Scaffold_PCL$_{500}$	8.68 ± 0.08	−1.13	8.61 ± 0.14	0.05	2.62 ± 0.09	−4.89	1.000 ± 0.033	−24.98	0.826 ± 0.033	17.37
Scaffold_PCL$_{500}$/Inu10	8.62 ± 0.09	−0.44	8.63 ± 0.09	−0.23	2.62 ± 0.06	−4.98	0.939 ± 0.032	−17.43	0.856 ± 0.042	14.43
Scaffold_PCL$_{500}$/Inu20	8.60 ± 0.12	−0.23	8.61 ± 0.17	−0.03	2.67 ± 0.05	−6.67	0.918 ± 0.039	−14.77	0.843 ± 0.041	15.71

The spectra revealed a marked reduction in the intensity of C═C-related bands, particularly at 1635 cm^{-1} (C═C stretching) and 815 cm^{-1} (C═C bending), confirming the consumption of methacrylate double bonds during photopolymerization and their involvement in network formation.

To complement this qualitative assessment, the degree of conversion (DC%) of methacrylate groups was quantitatively calculated by comparing the intensity of the 815 cm^{-1} peak relative to the 1150 cm^{-1} reference band, before and after printing. As shown in Table 4, all resin formulations exhibited high conversion efficiencies, with DC% values ranging from 74.93% to 96.06%, indicating effective crosslinking under the selected SLA printing conditions. Resins based on PCL$_{300}$ consistently showed higher conversion compared to their PCL$_{500}$ counterparts, likely due to their shorter chain length and higher density of reactive end groups. The incorporation of INUMA was associated with a slight reduction in DC%, particularly at higher concentration.

The extent of crosslinking directly affects the rigidity and structural stability of the scaffold, properties that are particularly relevant for bone tissue engineering, where mechanical strength and durability are essential. Moreover, inadequate polymerization may result in residual unreacted monomers, which are known to exhibit cytotoxic effects.[38] The high DC% values recorded across all tested samples suggest efficient curing and a minimal presence of unreacted species.

To further investigate the structural properties and crystallinity of the PCL$_{300}$- and PCL$_{500}$-based scaffolds, Raman spectroscopy was performed. Several distinctive peaks were identified in all scaffolds, corresponding to PCLTMA crystalline domains:

– 1280 cm^{-1} and 1306 cm^{-1} assigned to ω(CH) stretching vibration;

– 1450 cm^{-1} and 1466 cm^{-1} assigned to δ(CH$_2$) stretching;[66]

– 2800–3200 cm^{-1} due to νCH stretching, characteristic of the PCLTMA crystalline fraction[43,67] (Fig. 4).

Additionally, a broad peak at 865 cm^{-1} was observed in all samples, confirming the presence of an amorphous phase.[43]

To determine the degree of the crystallinity in the scaffolds, the C═O stretching band (1700–1750 cm^{-1}) was deconvoluted into two Gaussian curves, one centered at 1724 cm^{-1}, which corresponds to the crystalline phase, and one centered at 1732 cm^{-1}, which corresponds to the amorphous domain[43] (Fig. 4a, insets). For Scaffold_PCL$_{300}$/Inu10, the crystalline fraction (X_c) was found to be around 54% whereas the amorphous phase (X_a) was found to be 46%. In the case of Scaffold_PCL$_{300}$/Inu20, X_c was 52% and X_a was 48%. These values suggest a balanced microstructure where rigid crystalline domains and flexible amorphous regions coexist. A crystallinity around 50% typically represents an optimal trade-off between mechanical strength and flexibility, as higher crystalline content enhances rigidity and thermal stability, while the amorphous phase contributes to ductility and toughness.[68]

Furthermore, the crystallinity of the matrix significantly influences the drug release profile, with crystalline materials releasing drugs more slowly than their amorphous counterparts.[69–71] In our study, both Scaffold_PCL$_{300}$/Inu10 and Scaffold_PCL$_{300}$/Inu20, with similar crystalline and amorphous fractions, may provide a controlled and sustained drug release over time, making them suitable for long-term therapeutic applications while preserving scaffold stability.

Raman analysis also revealed peaks attributed to photoabsorber residues, specifically β-carotene, which was incorporated into the resin formulation. Peaks corresponding to the β-carotene's polyene chain vibrations were identified at:

– 1156 cm^{-1} → assigned to in-phase υ(C–C);

– 1525 cm^{-1} → assigned to polyene chain υ(C═C) stretching.[72,73]

To complete the physiochemical characterization, TGA analysis was performed to evaluate the thermal stability of the scaffolds compared to their liquid resin precursors. TGA results showed minimal mass loss at around 200 °C, likely due to residual non-crosslinked fractions,[38] and primary degradation onset at 480 °C, as determined by the first derivative of the thermograms. The higher degradation temperature of the crosslinked scaffolds, compared to the liquid resin, suggests

Table 4 Degree of conversion (DC) of the different resins after the 3D printing process. The DC was calculated by comparing the FTIR spectra of the resins and the corresponding scaffolds

Name	Degree of conversion (DC%)
PCL$_{300}$	96.06
PCL$_{300}$/Inu10	95.58
PCL$_{300}$/Inu20	87.14
PCL$_{500}$	79.87
PCL$_{500}$/Inu10	78.96
PCL$_{500}$/Inu20	74.93

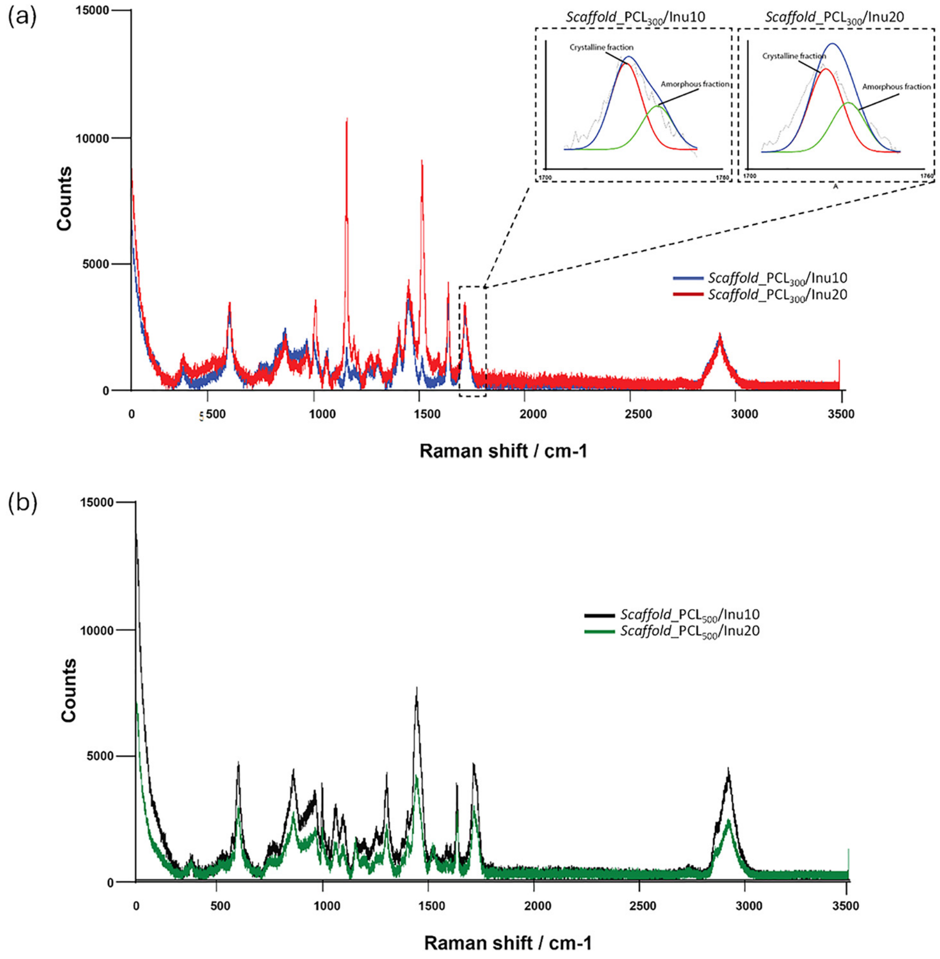

Fig. 4 Raman spectra of PCL_{300}-based scaffolds, with the inset showing the Gaussian deconvolution of the 1700–1750 cm^{-1} region (a). Raman spectra of PT500-based scaffolds (b).

that photopolymerization significantly improves thermal resistance, according to previous studies.[59,74]

Surface topography and morphology. SEM analysis provided detailed insights into the surface morphology and microscale structure of the scaffolds (Fig. 5 and Fig. S14). All formulations exhibited a uniform and regular surface, devoid of major defects or irregularities, indicating a homogeneous photopolymerization process.

Notably, scaffolds containing both PCLTMA and INUMA exhibited spherulitic crystal formation (Fig. 5 and Fig. S14), a feature previously reported in hybrid PCL scaffolds blended with an inulin-*g*-polylactide copolymer.[75] Spherulite formation in polymeric blends is commonly attributed to crystallization occurring in confined environments, where differences in polymer solidification rates create spatial constraints that influence crystallization pathways.[76] In this study, the presence of spherulites is likely a consequence of the distinct polymerization dynamics of PCLTMA and INUMA, which generate localized confinement zones that promote PCL crystallization. This finding supports the hypothesis that the hybrid blending of PCLTMA and INUMA plays a key role in shaping scaffold microtopography and microstructure.

This surface topography was investigated through roughness analysis using AFM. The results suggested that the incorporation of INUMA may contribute to an increase in both average roughness (SA) and root mean square roughness (SQ) in PCL_{300}- and PCL_{500}-based hybrid scaffolds (Fig. 6), with no significant difference between Scaffold_PCL_{300}/Inu10 and Scaffold_PCL_{300}/Inu20 or between Scaffold_PCL_{500}/Inu10 and Scaffold_PCL_{500}/Inu20.

To gain deeper insight into the surface topography of the scaffolds, additional AFM-derived roughness parameters were assessed, including skewness (SSK), kurtosis (SKU), developed interfacial area ratio (SDR), root mean square gradient (SDQ), and peak-peak height (Fig. S15). These advanced metrics provided a more detailed characterization of surface features, complementing the information obtained from SA and SQ.

The SSK parameter, which quantifies the asymmetry of the height distribution, revealed that all scaffolds, except for Scaffold_PCL_{500}/Inu20, exhibited symmetrical profiles, with

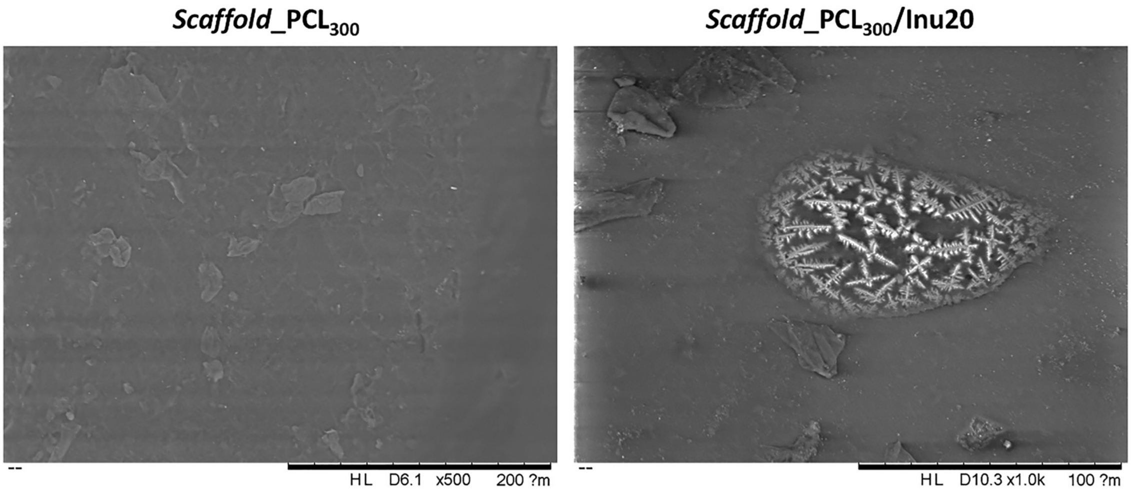

Fig. 5 SEM micrographs of 3D printed scaffold surface.

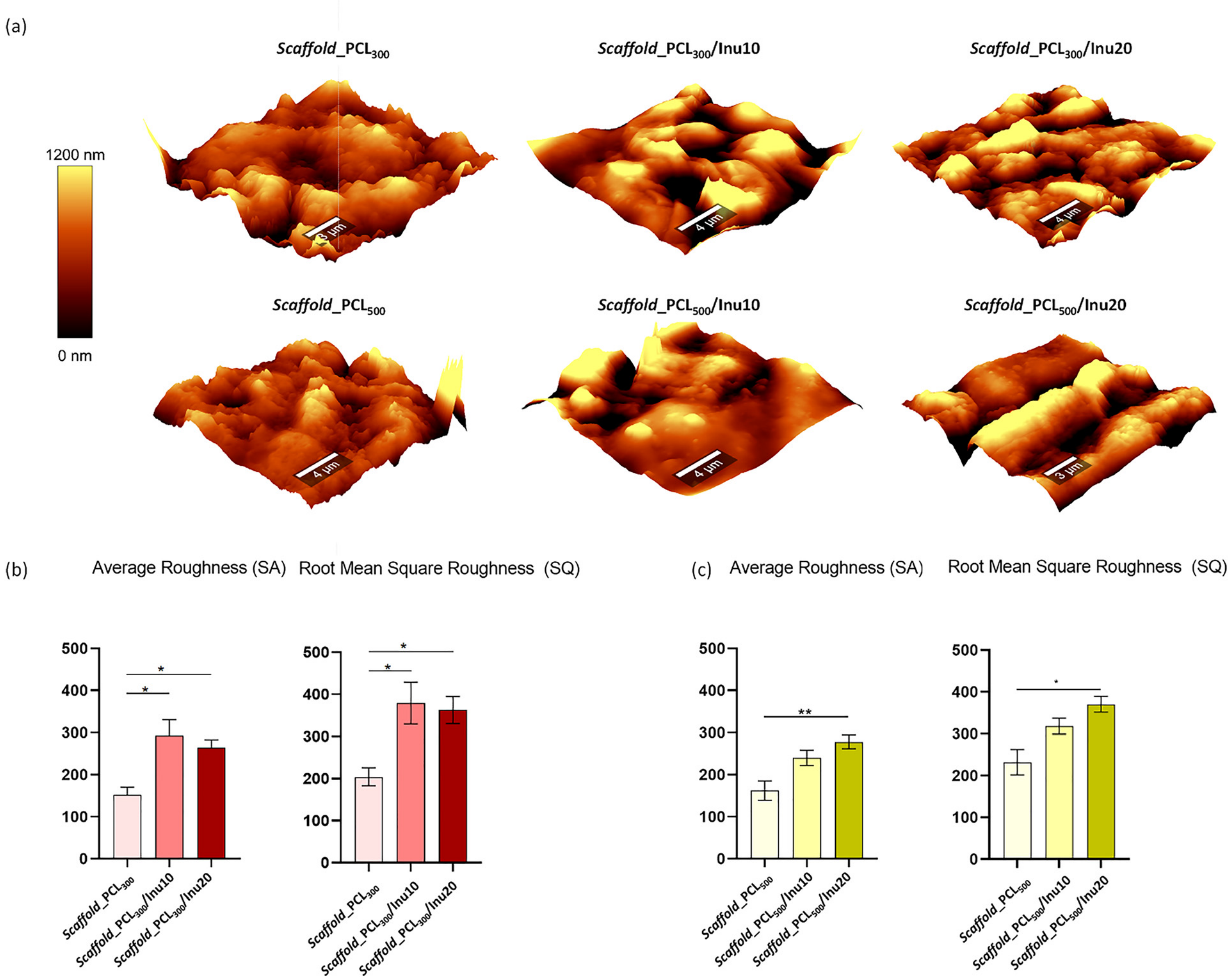

Fig. 6 Scaffold surface roughness evaluated by AFM: representative topographic images (a); average roughness (SA) and root mean square roughness (SQ) for PCL$_{300}$ (b) and PCL$_{500}$ series (c). Data are reported as mean ± SD (n = 3). Statistical analysis was performed using Kruskal–Wallis test followed by Dunn's *post hoc* test for multiple comparisons. The mean rank of each column was compared with the mean rank of the control group (*: $p < 0.05$, **: $p < 0.01$).

values closer to zero (Fig. S15a). This suggests a relatively balanced distribution of surface peaks and pits in most samples. SDR evaluation supported the influence of INUMA on surface complexity: scaffolds containing INUMA exhibited

Table 5 Young's modulus of scaffolds. Data expressed as mean ± SD ($n = 3$)

Name	Young's modulus (MPa)
Scaffold_PCL$_{300}$	5.00 ± 0.43
Scaffold_PCL$_{300}$/Inu10	6.37 ± 0.42
Scaffold_PCL$_{300}$/Inu20	6.93 ± 0.85
Scaffold_PCL$_{500}$	3.12 ± 0.85
Scaffold_PCL$_{500}$/Inu10	4.08 ± 0.15
Scaffold_PCL$_{500}$/Inu20	5.46 ± 0.74

higher values, indicating a greater effective surface area due to increased nanoscale texture (Fig. S15c). This reinforces the idea that INUMA enhances surface structuring, likely because of phase separation at the nanoscale.

Overall, these findings suggest that INUMA incorporation modulates scaffold topography by increasing surface complexity, a feature that may enhance cell–material interactions and improve performance in tissue engineering applications.[77]

Mechanical properties. Mechanical properties are critical for scaffolds intended for bone implants, as they must provide adequate mechanical support and structural integrity to withstand the loads and stresses present in the bone tissue environment.[78,79] The mechanical performance of the scaffolds was assessed through compression tests, with the resulting stress–strain curves and Young's modulus values reported in Fig. S16 and Table 5, respectively.

All scaffolds exhibited Young's modulus values ranging from 3.12 and 6.93 MPa, which fall within the wide range of human trabecular bone (1–5000 MPa).[80,81] Scaffolds from the PCL$_{300}$ series demonstrated higher Young's modulus values compared to those from the PCL$_{500}$ series. Specifically, Scaffold_PCL$_{300}$ exhibited a Young's modulus of 5.00 ± 0.43 MPa, while the Scaffold_PCL$_{500}$ showed a lower value of 3.12 ± 0.85 MPa. This difference is attributed to the lower molecular weight of PCLTMA (300 Da) and aligns with the higher degree of conversion detected by FTIR, indicating a denser crosslinked network. The increased crosslinking density reinforces the material against applied stress and facilitates even stress distribution across the polymer network, resulting in a stiffer and more robust scaffold.[51] These results align with findings in the literature, where the compressive Young's modulus increases linearly with crosslinking density,[82] and are consistent with previous studies on methacrylate-based PCL networks.[48,51]

The incorporation of INUMA was associated with a progressive increase in Young's modulus. For the PCL$_{300}$ series, scaffolds with 10% and 20% INUMA exhibited Young's modulus values of 6.37 ± 0.42 MPa and 6.93 ± 0.85 MPa, respectively. In the PCL$_{500}$ series, Young's modulus increased from 4.08 ± 0.15 MPa at 10% INUMA to 5.46 ± 0.74 MPa at 20% INUMA. Such findings likely arise from a combination of factors. On one hand, INUMA carries methacrylate groups that can undergo photopolymerization, potentially leading to interpenetrating networks with the PCLTMA backbone. This may contribute to partial crosslinking and increased matrix cohesion. These results are in line with the work of Cheng *et al.*, who demonstrated improved mechanical properties in PCL diacrylate scaffolds upon incorporation of a second photocurable polymer, such as PEGDA.[53] On the other hand, INUMA may also exert a physical reinforcement effect. Being only partially solubilized in the resin, undissolved INUMA domains could act as dispersed fillers within the scaffold structure, contributing to the overall stiffness. Similar filler-like behavior of natural polysaccharides or particles has been reported in several studies on composite biomaterials, where physical dispersion within the polymer matrix produces an increase of the Young's modulus even without full chemical integration.[83]

Wettability. Wettability is a fundamental parameter for evaluating the applicability of scaffolds in tissue engineering, as enhanced surface hydrophilicity promotes protein adsorption,[84] improves the absorption of growth factors, and reduces platelet activation.[38] These factors contribute to better cell–material interactions and increased biocompatibility.[85] Wettability is typically quantified through static aqueous contact angle measurements, where surfaces with a contact angle below 90° are considered hydrophilic, while those with an angle above 90° are classified as hydrophobic.[86]

In this study, scaffolds composed solely of PCLTMA exhibited contact angles of 76.13 ± 1.43° for Scaffold_PCL$_{300}$ and 79.67 ± 5.36° for Scaffold_PCL$_{500}$, with no significant difference between the two formulations. These values are consistent with similar studies in the literature, which report acrylate derivatives of PCL having comparable contact angles.[23,53] As expected, the addition of INUMA, a more hydrophilic component due to its abundance of free hydroxyl groups which can facilitate hydrogen bonding with water, significantly increased scaffold wettability, as evidenced by a decrease in water contact angle proportional to INUMA content. The scaffolds containing PCLTMA : INUMA in an 80 : 20 weight ratio (Scaffold_PCL$_{300}$/Inu20 and Scaffold_PCL$_{500}$/Inu20) achieved contact angle values of 56.78 ± 1.40° and 59.80 ± 2.00°, respectively, confirming the effect of INUMA on scaffold surface hydrophilicity.

Swelling capacity. Swelling ability, defined as the fractional increase in mass due to solvent absorption, plays a critical role in body fluid absorption, cell attachment, and nutrient transfer within the scaffold after implantation **https://pubs.rsc.org/en/content/articlelanding/2021/qm/d1qm00583a/unauth**.[87] As illustrated in Fig. 7, scaffolds composed solely of PCLTMA exhibited a low fluid uptake percentage after 3 days (5.05 ± 0.60 for Scaffold_PCL$_{300}$ and 6.15 ± 0.62% for Scaffold_PCL$_{500}$). This observation aligns with the literature, which describes PCL as a poorly hydrophilic material.[19] Incorporating INUMA markedly enhanced the swelling capacity of the scaffolds. Scaffolds containing 10% INUMA (Scaffold_PCL$_{300}$/Inu10 and Scaffold_PCL$_{500}$/Inu10) exhibited a fluid uptake percentage of 12.15 ± 1.08% and 11.19 ± 0.68%, respectively, while scaffolds with 20% INUMA achieved a maximum fluid uptake of 17.87 ± 0.30% for Scaffold_PCL$_{300}$/Inu20 and 17.08 ± 1.09% for Scaffold_PCL$_{500}$/Inu20. Over time, these scaffolds showed a slight decrease in swelling, stabilizing at around 11% at 21 days (11.68 ± 0.59% for Scaffold_PCL$_{300}$/Inu20 and 10.66 ± 0.39%

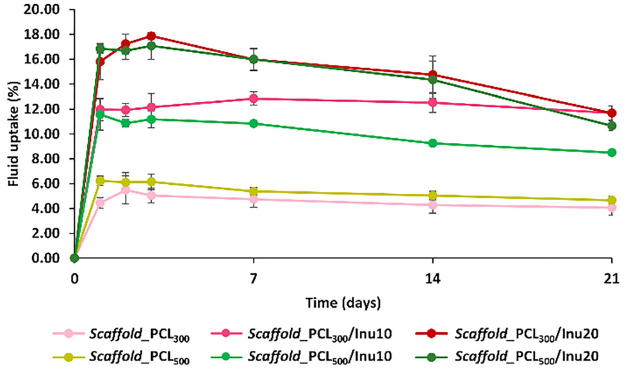

Fig. 7 Fluid uptake capacity of scaffolds incubated in PBS pH 7.4 at 37 °C over 21 days. Data are expressed as mean values (n = 3), with error bars representing standard deviation.

for Scaffold_PCL$_{500}$/Inu20), likely due to the onset of the degradation process.

These results confirm a strong correlation between INUMA content and increased swelling ability, which is attributed to the enhanced wettability of the resulting 3D printed scaffolds.

***In vitro* degradation.** Biodegradability is fundamental requirement for scaffolds intended for tissue engineering, as they are not designed to be permanent implants but should instead be gradually replaced by newly formed extracellular matrix.[23]

In this study, scaffold biodegradation was evaluated through two complementary *in vitro* experiments: (i) incubation in PBS, a condition recommended by ASTM F1635-11 standards and commonly used to simulate physiological environments; and (ii) exposure to NaOH solution, a highly alkaline medium employed as an accelerated degradation model to rapidly assess the comparative degradation behaviour of PCL[88] and its (meth)acrylate derivatives.[51] In PBS, the scaffolds exhibited a slow and controlled degradation profile over six weeks, retaining 94.69 ± 0.74% and 92.63 ± 1.24% of their initial mass for PCLTMA$_{300}$ and PCLTMA$_{500}$-based scaffolds (Fig. 8a), respectively. These values are lightly higher than those typically reported for linear PCL, likely due to the presence of methacrylate groups, which alter the degradation dynamics.[17,89] Conversely, under accelerated conditions (NaOH), a more rapid breakdown was observed, with residual weights dropping to 53.35 ± 5.73% for Scaffold_PCL$_{300}$ and 49.76 ± 3.06% for Scaffold_PCL$_{500}$ after just two weeks (Fig. 8b).

Both experimental conditions revealed a consistent trend: degradation rate increased with increasing molecular weight of the PCL precursor. This behaviour is specific to photopolymerizable systems, where lower molecular weight correlates with a higher density of methacrylate groups.[13,51] As confirmed by FTIR analysis (Table 4), this leads to higher conversion rates during photopolymerization and thus a denser crosslinked network. These highly crosslinked domains are composed of saturated, nondegradable, and relatively hydrophobic segments, which hinder water uptake and diffusion. As a result, ester bond hydrolysis in the PCL backbone is limited, slowing the overall degradation process.[51,90]

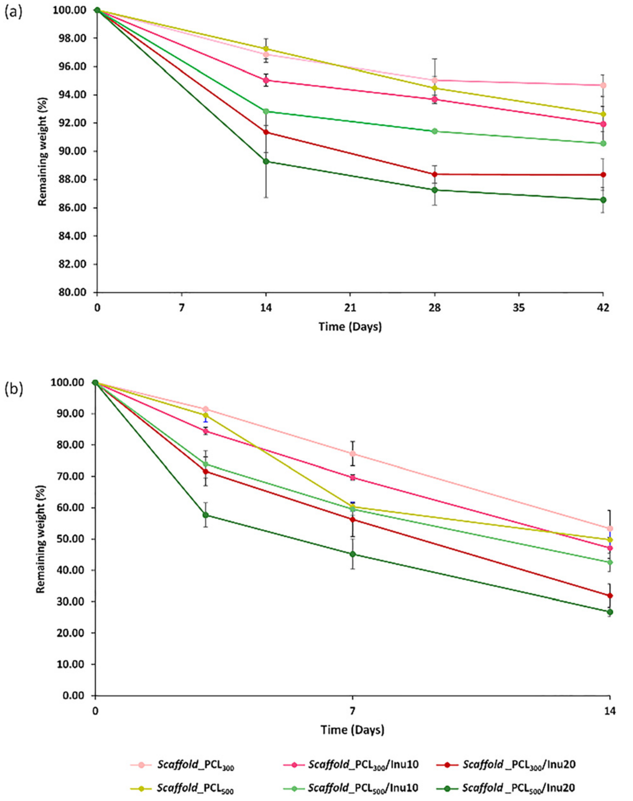

Fig. 8 *In vitro* biodegradation profile of 3D printed scaffolds after incubation in PBS, pH 7.4 for 42 days (a) and in NaOH 1 M for 14 days (b). Biodegradation was evaluated as percentage weight loss over time. Data are expressed as mean values (n = 3), with error bars representing standard deviation.

This finding is in contrasts with the behaviour of non-crosslinked polymers, where degradation typically slows as molecular weight increases.[91]

The incorporation of INUMA significantly accelerated scaffold degradation. Scaffolds containing the highest INUMA content (Scaffold_PCL$_{300}$/Inu20 and Scaffold_PCL$_{500}$/Inu20) showed mass loss approximately twice as high as those composed solely of PCLTMA. This outcome aligns with expectations, given INUMA's greater hydrophilicity and enhanced ability to interact with fluids. The ability to tune the degradation rate highlights INUMA's role in addressing one of the main limitations of PCL, with important implications for tissue engineering applications, where prolonged placement of materials within the body may lead to a chronic foreign body reaction, fibrous encapsulation,[13] and impaired osteointegration or delayed new bone formation.[92] Future studies may investigate formulations with increased INUMA content, potentially optimizing the resin matrix through tailored processing strategies or alternative solvent systems. This could enhance the dispersion and solubilization of INUMA, further tuning scaffold degradation rates and expanding their functional versatility for regenerative applications.

Fabrication and characterization of drug-*loaded scaffolds*. To develop scaffolds loaded with RAL, we selected the hybrid

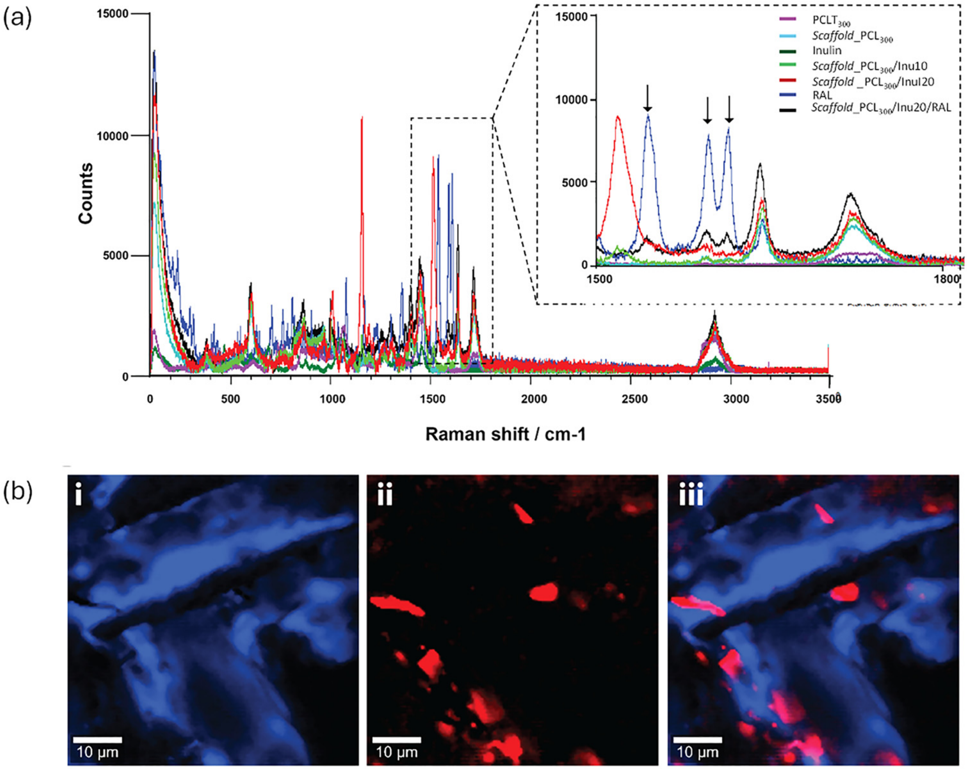

Fig. 9 Raman spectra of Scaffold_PCL*300*/Inu20/RAL with zoom-in on the 1500–1800 cm^{-1} spectral range showing distinctive RAL peaks (black arrows) (a). Raman maps illustrating the spatial distribution of PCLTMA (blue) and RAL (red) (b).

resin composition that demonstrated the best overall performance during preliminary studies. The blend containing $PCLTMA_{300}$ and 20% INUMA (Resin/Scaffold_PCL_{300}/Inu20) was identified as the optimal candidate.

This formulation exhibited superior mechanical resistance, attributable to the high crosslinking density provided by the low-molecular weight PCLTMA and the reinforcing effect of INUMA. Additionally, the blend showed enhanced wettability and swelling capacity due to the hydrophilic properties of INUMA, along with a favourable degradation profile, reflecting a controlled and predictable breakdown suitable for biomedical applications. These attributes established Scaffold_PCL_{300}/Inu20 as the ideal scaffold composition for the incorporation of the selected drug.

RAL was incorporated into the Resin_PCL_{300}/Inu20 *via* direct dissolution at a concentration of 1% w/w, aiming for a drug loading of approximately 1 mg per construct. The resulting drug-loaded resins and scaffolds (Resin/Scaffold_PCL_{300}/Inu20) were subjected to the same comprehensive characterization as the blank scaffolds to ensure consistency and reliability.

Characterization of the drug-loaded resins (viscosity measurements, TGA analysis, FTIR spectroscopy, and optical characterization) yielded results comparable to the blank resins, confirming that the addition of RAL did not alter the overall physicochemical properties (Fig. S18).

To verify the presence of RAL on the scaffold surface, Raman spectroscopy was employed. In agreement with previous reports, the Raman spectrum of RAL displayed three distinctive peaks around 1280 cm^{-1}, due to CH_2 wagging, and two peaks around 1590 cm^{-1} and 1615 cm^{-1}, related to the C$=$C stretching of the aromatic rings, which are typically found in the crystalline form of RAL.[93] Additionally, a peak at 1545 cm^{-1}, assigned to a C_6–H deformation and indicative of chloride anion interaction,[94] was also observed in Scaffold_PCL_{300}/Inu20/RAL, confirming the presence of RAL (Fig. 9a, black arrows).

Raman mapping allowed the visualization of RAL on the scaffold surface. In the maps, the PCLTMA matrix appears in blue, while RAL is highlighted in red (Fig. 9b).

The presence of RAL within the scaffolds also influenced their surface topography. AFM image analysis revealed the formation of point-like crystalline aggregates embedded in the scaffold surface, likely resulting from the crystallization of RAL within the polymer matrix. This morphological alteration was particularly reflected in the skewness (SSK) values, which shifted from values close to zero in the blank scaffolds to approximately +1 in the RAL loaded samples, suggesting the presence of crystalline RAL domains (Fig. S15a). This interpretation was further supported by the kurtosis (SKU) values, which were consistently greater than 3 for the drug-loaded scaffolds, indicating a spiked surface profile characterized by sharp, narrow features such as pits or steep transitions (Fig. S15b), and was also consistent with the increased peak–peak height (Fig. S15e). The emergence of such surface features may influence not only mechanical anchoring at the micro–nanoscale,[95] but also early-stage cell–material interactions by providing topographical cues that promote cell adhesion.[77]

Table 6 Drug loading and efficiency of resins and scaffolds. Data expressed as mean ± SD (n = 3)

	Experimental drug loading (w/w%)	Theoretical drug loading (w/w%)	Loading efficiency (%)
Resin_PCL_{300}/Inu20/RAL	0.98 ± 0.05	1.00	98.00 ± 4.87
Scaffold_PCL_{300}/Inu20/RAL	0.97 ± 0.01	1.00	96.86 ± 1.15

Drug loading and efficiency studies showed that the drug content in both the resin and the scaffold closely matched the theoretical value (Table 6), confirming that SLA, when conducted under optimized conditions—such as the careful selection of starting materials, formulation agents (*e.g.*, photoinitiators and photoabsorbers), fine-tuned photopolymerization parameters, and post-printing processes—can achieve high drug loading efficiency.

Unlike extrusion-based 3D printing techniques, SLA eliminates pre-processing steps (*e.g.*, extrusion) and cartridge-based transfers, which can result in material loss. Finally, since the process occurs within a resin tank, unpolymerized resin can be recovered, further reducing waste and improving overall efficiency.

Further characterization revealed no significant differences in mechanical performance between Scaffold_PCL_{300}/Inu20/RAL and the corresponding blank scaffolds. Young's modulus was slightly higher in drug-loaded scaffolds (7.11 ± 0.34 MPa *vs.* 6.93 ± 0.85 MPa for Scaffold_PCL_{300}/Inu20), indicating that RAL does not compromise mechanical integrity.

The contact angle increased modestly from 56.78 ± 0.40° (blank scaffold) to 61.78 ± 3.42°, likely due to the hydrophobic nature of RAL. However, this change did not significantly affect fluid absorption or degradation rates, which remained consistent with the blank scaffold properties (Fig. S19 and S20).

Finally, the drug release profile exhibited an initial release of approximately 30% within the first 24 hours, followed by a slow, sustained release, reaching 60% over the study period (Fig. 10). While this initial phase might suggest a burst phenomenon, further kinetic analysis indicated otherwise. To gain deeper insight into the release mechanism, the release profiles were fitted to various mathematical models (Table S4). Among these, the Weibull model provided the best fit (R^2 = 0.9680), followed by the Korsmeyer–Peppas model (R^2 = 0.9094), both pointing to diffusion as the governing mechanism. Importantly, the Weibull shape parameter (b = 0.23) was well below unity, consistent with a decelerating release process and not with the accelerating kinetics typically associated with burst release ($b > 1$). In addition, linearization of the early release data (cumulative release % *vs.* $\sqrt{\text{time}}$) did not show a significant intercept, indicating that the observed release originated from diffusion through the matrix rather than from superficial desorption. Residual analysis of the Weibull fit (Fig. S21) further confirmed that the early phase was adequately captured without systematic deviations. On this basis, the ~30% released in the first 24 h could be ascribed to the initial stage of a diffusion-controlled release, rather than to a true burst event. Moreover, in agreement with other recent works on photo-crosslinked polyester-based systems,[96] our data suggest the potential for a secondary release phase: while drug diffusion may initially be limited by highly crosslinked domains that hinder fluid access and slow ester bond hydrolysis, a secondary release phase may gradually emerge as the matrix degrades over time. Such second release mechanism can be anticipated by regulating composition as well as printing

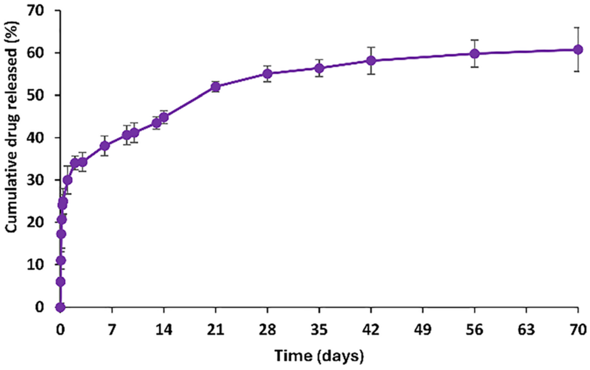

Fig. 10 Drug release profile from Scaffold_PCL_{300}/Inu20/RAL in PBS at 37 °C, over 10 weeks. Data are expressed as mean values (n = 3), with error bars representing standard deviation.

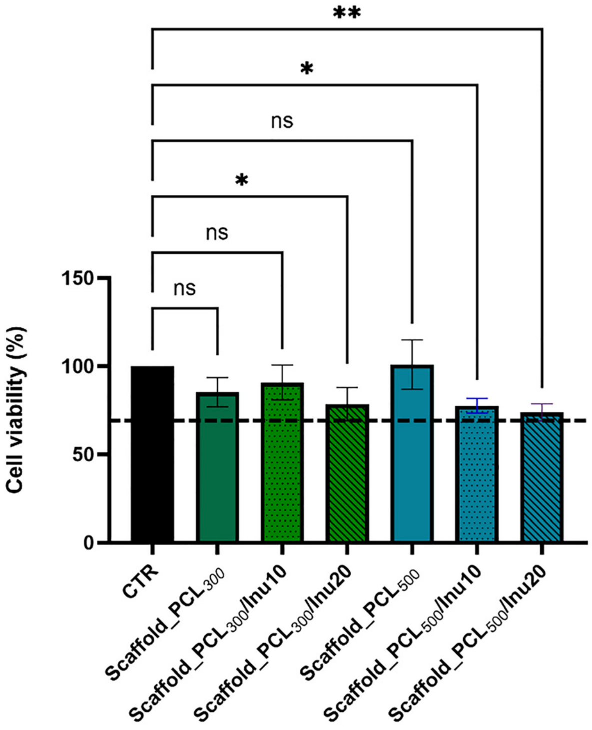

Fig. 11 Indirect cytotoxicity assessment on hMSCs-P8 using AlamarBlue assay. Results were normalized to the control (CTR) and expressed as a percentage of cell viability. A horizontal dashed line indicates the 70% cytocompatibility threshold according to ISO 10993-5. Data are expressed as mean values (n = 3), with error bars representing standard deviation. Statistical analysis was performed using Kruskal–Wallis test followed by Dunn's *post hoc* test for multiple comparisons (*: $p < 0.05$, **: $p < 0.01$, ns: not significant).

geometry[96,97] and could help compensate for the decline in release rate, thereby facilitating sustained release of the remaining drug fraction over an extended period.

Evaluation of *in vitro* biological performance. *In vitro* studies were conducted to evaluate the cytocompatibility of the scaffolds, a crucial parameter for assessing their ability to support cellular growth and promote tissue regeneration.

Initially, cytocompatibility was indirectly assessed using the eluates obtained from the scaffolds. The results showed no significant reduction in cell viability compared to the control, except for Scaffold_PCL$_{500}$/Inu10, Scaffold_PCL$_{500}$/Inu20, and Scaffold_PCL$_{300}$/Inu20 (Fig. 11). However, since cell viability remained above the 70% threshold, as defined by ISO 10993-5: 2009 standards,[98] it can be concluded that the scaffolds were non-cytotoxic after 24 hours of incubation.

A subsequent direct cytocompatibility assessment was performed by seeding hMSCs directly onto the scaffolds and monitoring their viability over 21 days. All blank scaffolds provided excellent support for cell growth and viability throughout the culture period. Notably, PCL$_{300}$ series scaffolds, especially those containing INUMA at the highest concentration (Scaffold_PCL$_{300}$/Inu20), showed a significant increase in cell proliferation by day 7, indicating enhanced support for cell adhesion and growth (Fig. 12).

In contrast, the drug-loaded scaffolds (Scaffold_PCL$_{300}$/Inu20/Ral), showed reduced cell viability compared to their blank counterpart (Scaffold_PCL$_{300}$/Inu20). While cell viability remained above 70% at 24 and 72 hours, a decline was observed at day 7, followed by recovery at day 14 (Fig. 12). This transient reduction in cell viability is likely due to the high

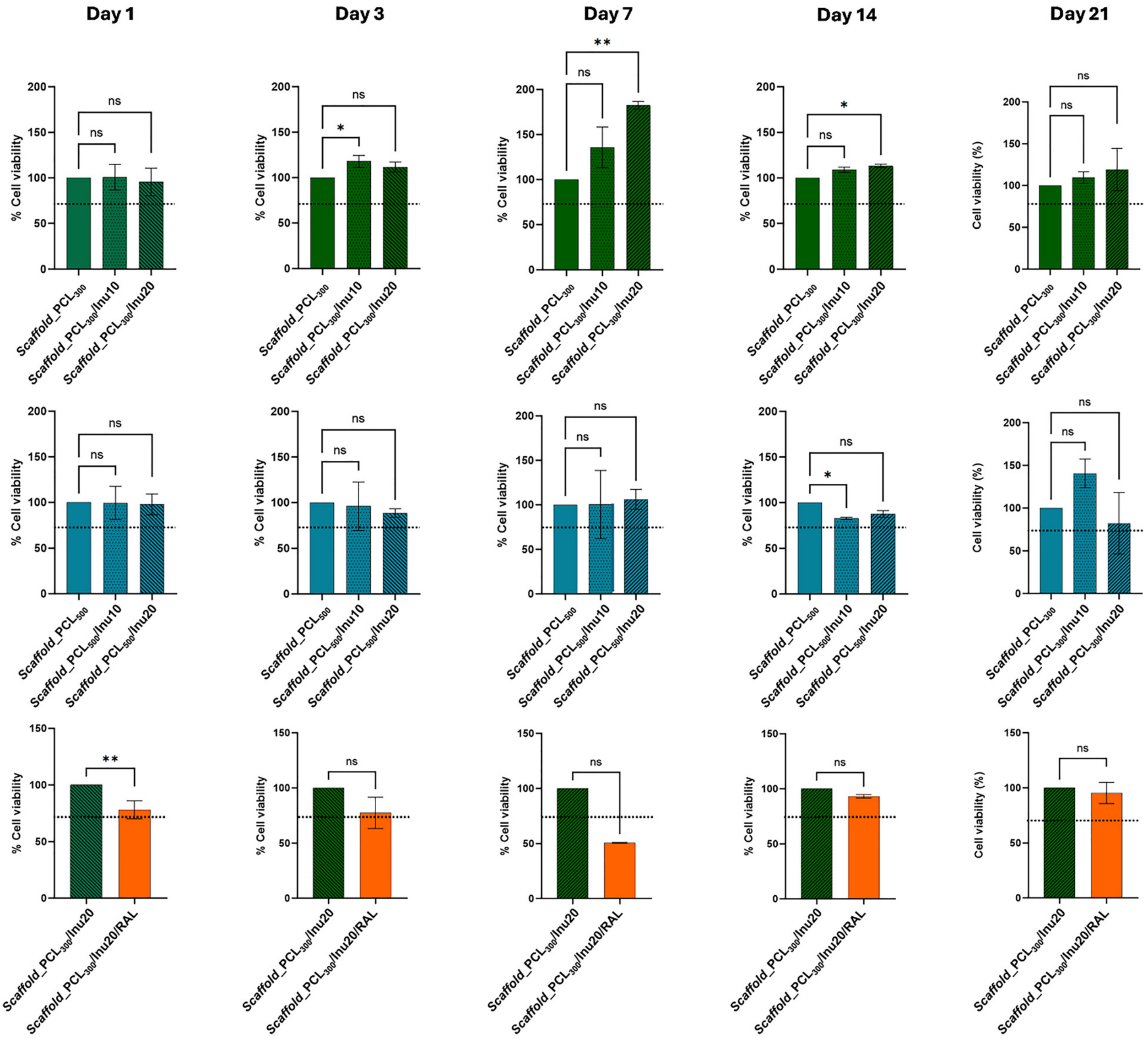

Fig. 12 Cell viability of hMSCs-P4 over time using the AlamarBlue assay. Results were normalized to the control scaffolds (Scaffold_PCL$_{300}$, Scaffold_PCL$_{500}$ and Scaffold_PCL$_{300}$/Inu20) and expressed as a percentage of cell viability. A horizontal dashed line indicates the 70% cytocompatibility threshold according to ISO 10993-5. Data are expressed as mean values (n = 3), with error bars representing standard deviation. Statistical analysis was performed using Kruskal–Wallis test followed by Dunn's *post hoc* test for multiple comparisons (*: $p \leq 0.05$, **: $p \leq 0.01$, ns: not significant).

initial drug release, which resulted in elevated RAL concentrations during the early culture phase, causing a temporary cytotoxic effect. However, the subsequent recovery in cell viability suggests that once the drug concentration stabilized, the scaffolds supported cell growth effectively. Cell adhesion and morphology were further evaluated by SEM analysis after 21 days of culture (Fig. 13). SEM images revealed that hMSCs successfully adhered to and spread across the surface of all scaffolds, forming extensive cytoplasmatic extensions. These morphological features suggest good interaction between the cells and the biomaterial, facilitating cell attachment, spreading, and integration.

To better explore the bioactive effects of raloxifene on cell behaviour—particularly viability, morphology, and differentiation—further studies were performed using SAOS-2 cells, a widely accepted osteosarcoma-derived cell line for evaluating osteogenic potential *in vitro*. An initial cytocompatibility analysis was carried out using an indirect assay with Calcein-AM staining (Fig. S22a and b). As shown in Fig. S22b, SAOS-2 cells exposed to conditioned media from the Scaffold_PCL$_{300}$/Inu20/RAL exhibited reduced viability at day 3 compared to the control (cells cultured on standard tissue culture plastic). This observation was corroborated by Alamar Blue assays (Fig. S23),

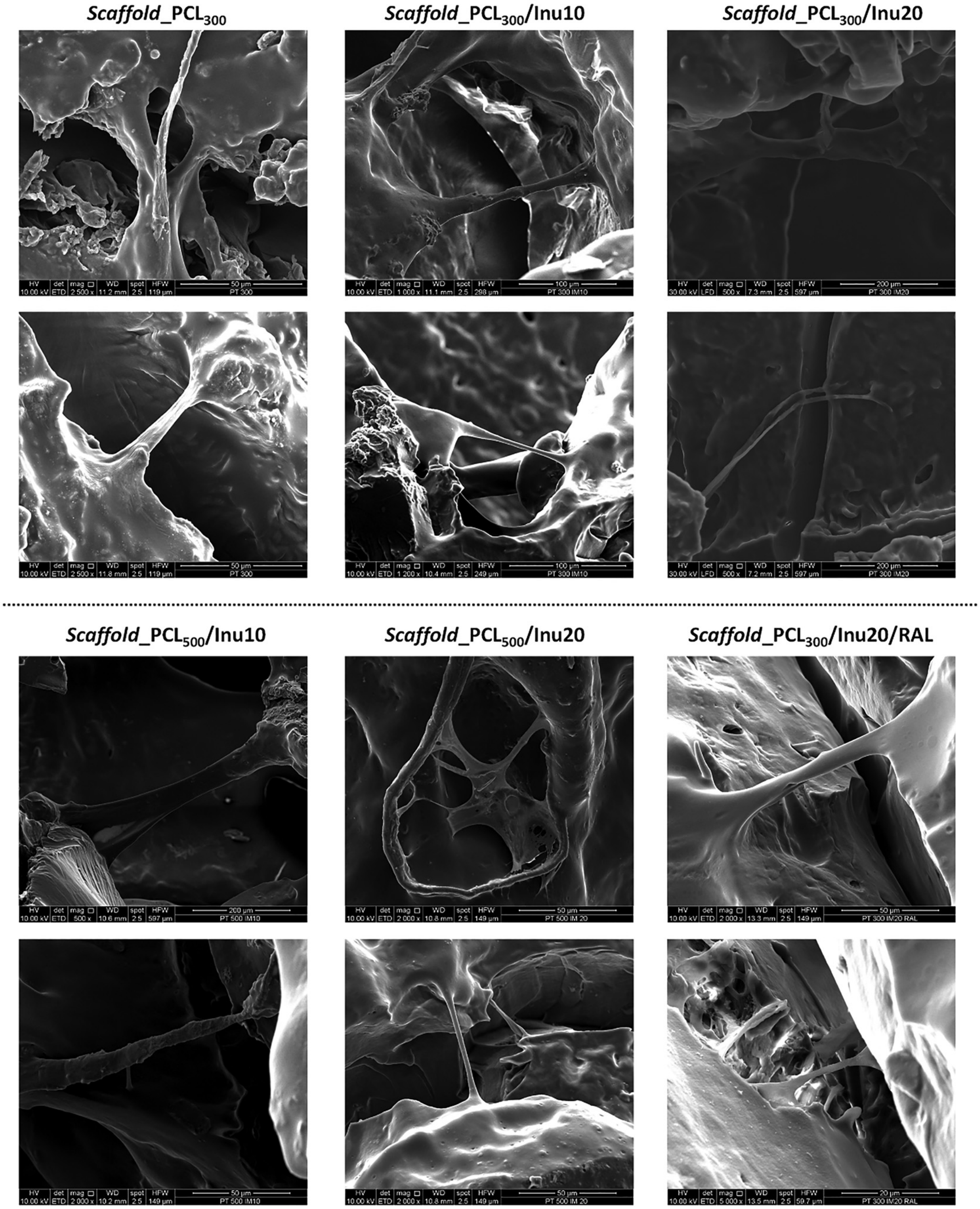

Fig. 13 SEM images of hMSCs cultured on scaffolds after 21 days of incubation.

which tracked viability over 14 days. While most scaffolds supported a steady increase in cell viability, the raloxifene-containing scaffold showed a transient decrease at days 3 and 7, followed by significant recovery at day 14.

This time-dependent trend suggests that the initial decline in metabolic activity was not caused by cytotoxicity, but rather reflects an early cellular response potentially associated with osteogenic commitment. Morphological analysis confirmed this interpretation: cells across all conditions appeared well-spread and healthy. Indeed, CellMask™ staining at days 7 and 14 supported these findings, showing increased cell density over time and uniformly spread cells without morphological abnormalities (Fig. 14a). Quantitative analysis of cell area (Fig. 15a) and perimeter (Fig. 15b) further demonstrated that conditioned media, including raloxifene, had no adverse effects on cell morphology. Osteogenic commitment was suggested by the expression of both early (collagen I, COL1) and late (osteocalcin, OCN) markers at day 7, even under basal conditions without osteogenic supplements.

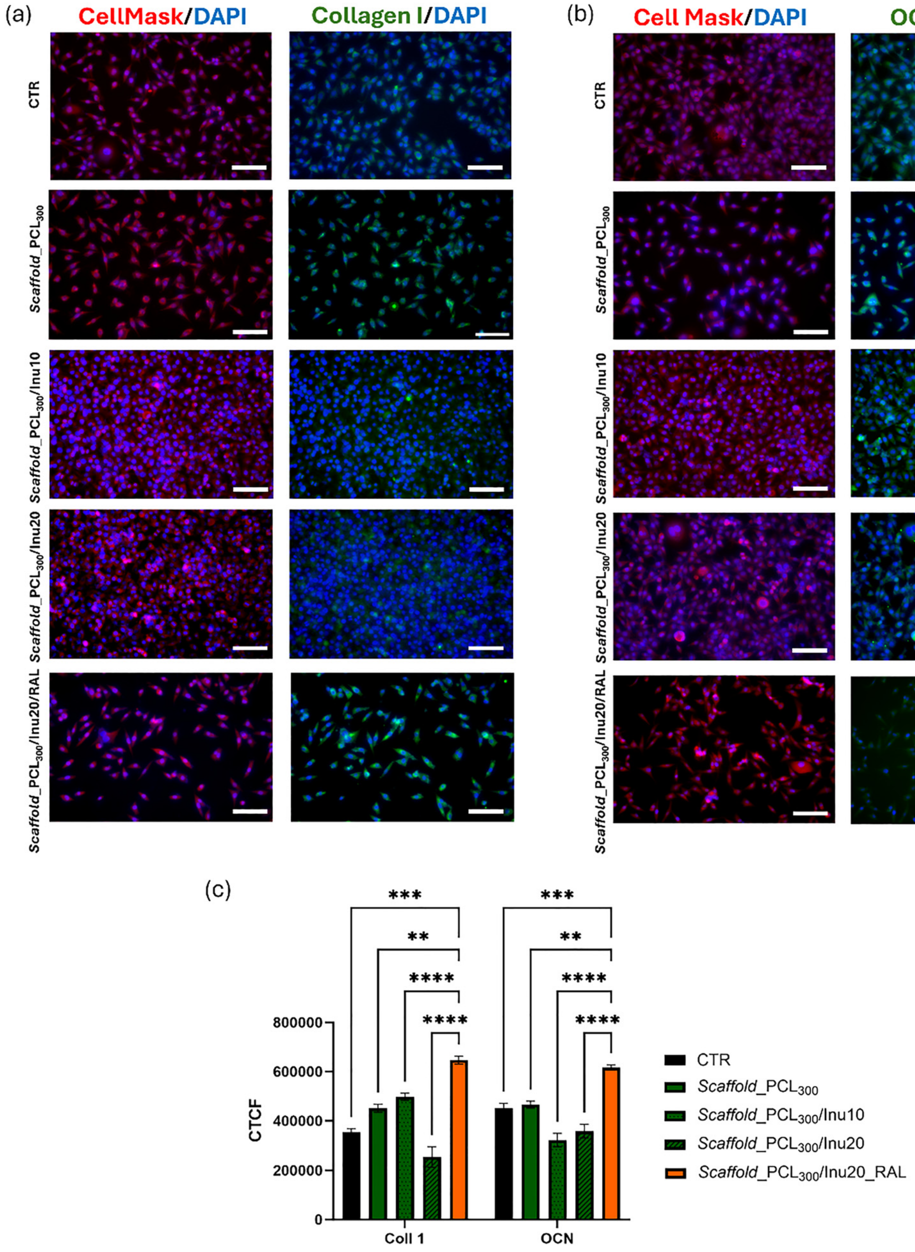

Fig. 14 Representative fluorescence microscopy images and quantitative analysis of osteogenic marker expression in SAOS-2 cells at 7 days. Merged fluorescence channels showing nuclei (DAPI, blue) and cell membranes (CellMask, red), alongside collagen type I (Col I, green) and DAPI (a). Additional merged images displaying DAPI (blue) with CellMask (red), alongside osteocalcin (OCN, green) with DAPI (blue). All images were acquired at 20× magnification. Scale bar: 100 μm (b). Quantification of corrected total cell fluorescence (CTCF) for collagen I and OCN, reported as mean ± SD ($n = 3$), with error bars representing standard deviation (c). Statistical significance was evaluated using two-way ANOVA; $^{****}p < 0.05$ was considered significant.

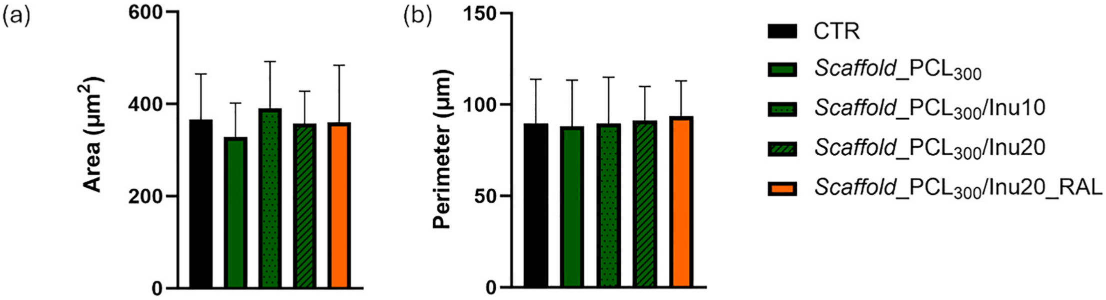

Fig. 15 Quantitative morphological analysis of SAOS-2 cells following exposure to scaffold eluates. Graph showing the average cell area (μm^2) measured after 7 days of culture (a). Graph reporting the average cell perimeter (μm) under the same conditions. Morphometric parameters were calculated using Fiji/ImageJ software from CellMask-stained images (b). Data are expressed as mean values (*n* = 3), with error bars representing standard deviation.

Immunofluorescence analysis at days 7 (Fig. 14) and 14 (Fig. S24) qualitatively confirmed expression of these markers. Additionally, quantitative analysis based on corrected total cell fluorescence (CTCF) at day 7 revealed a significant increase in COL1 and OCN signal intensities in cells treated with raloxifene-conditioned media (Fig. 14b). These findings indicate a potential pro-osteogenic effect of raloxifene, even in the absence of external osteoinductive stimuli.

This outcome is consistent with previous reports showing that raloxifene promotes osteogenic differentiation and matrix maturation *via* estrogen receptor–mediated signalling pathways. Altogether, the combined results from viability assays, morphological analysis, and marker expression support the hypothesis that the released raloxifene remains biologically active and may contribute to a pro-osteogenic effect *in vitro*.

The encouraging results obtained through indirect analyses of osteogenic markers provide a solid foundation for future investigations. Functional assays such as alkaline phosphatase (ALP) activity and late-stage mineralisation (*e.g.*, Alizarin Red staining) will be conducted in follow-up studies to fully validate the osteoinductive potential of the developed scaffolds and further substantiate the preliminary evidence observed in this work.

Conclusions

In this study, we successfully developed and optimized six distinct photopolymerizable resin compositions based on polycaprolactone trimethacrylate (PCLTMA) and methacrylated inulin (INUMA) to fabricate bone-mimicking scaffolds *via* resin-based 3DP technologies. The combination of careful resin formulation, including the selection of suitable photoinitiators and photoabsorbers, enabled the production of scaffolds with high fidelity to the digital designs, exceptional reproducibility, and structural precision, all critical parameters for BTE applications.

A comprehensive evaluation of the influence of PCLTMA molecular weight and INUMA concentration on scaffold properties revealed that low molecular weight PCLTMA promoted a higher extent of methacrylate conversion and thus the formation of a denser crosslinked network, resulting in superior mechanical performance and prolonged degradation profiles. Conversely, INUMA incorporation significantly enhanced surface hydrophilicity, swelling capacity, and degradation rates, while simultaneously providing mechanical reinforcement to the scaffold structure in the early stage.

Among the compositions studied, Scaffold_PCL$_{300}$/Inu20 was identified as the optimal resin blend for further functionalization due to its balanced mechanical strength, favorable degradation kinetics, and enhanced wettability. The incorporation of raloxifene hydrochloride at 1% w/w into this hybrid resin resulted in high drug loading efficiency and uniform distribution of the drug throughout the scaffold matrix. The drug release profile, characterized by a rapid initial release followed by a sustained release over 10 weeks, highlights the potential of these scaffolds for localized therapeutic applications in osteoporosis treatment.

The results of *in vitro* biological studies confirmed the cytocompatibility of the scaffolds, demonstrating their ability to support cell adhesion, proliferation, and viability. These findings suggest that further optimization of drug release profiles could enhance long-term cellular compatibility while maintaining therapeutic efficacy, paving the way for advanced multifunctional scaffolds. Moreover, the up-regulation of early and late osteogenic markers (collagen I and osteocalcin) in SAOS-2 cells exposed to scaffold eluates supports the hypothesis that the released raloxifene retains its biological activity and promotes a pro-osteogenic response. Although these results were obtained through indirect assays, they provide a solid foundation for future functional investigations, such as ALP activity and matrix mineralisation, that will be necessary to fully validate the osteoinductive potential of the developed system.

This research offers a valuable contribution to the field of BTE by expanding the range of compatible hybrid resins and presenting an innovative platform for combining high-precision 3DP with advanced drug delivery. The integration of functional biomaterials with customizable manufacturing techniques enables the creation of scaffolds that mimic bone architecture, enhance mechanical performance, and deliver therapeutic agents in a controlled manner.

In conclusion, this work lays a solid foundation for future exploration of hybrid SLA resins in BTE applications. The developed blank and drug-loaded scaffolds demonstrate the feasibility of creating multifunctional scaffolds that can be tailored to meet specific clinical needs, offering new opportunities in bone regeneration and personalized medicine.

Author contributions

Carmela Tommasino: investigation, methodology, data curation, formal analysis, writing – original draft, visualization. Carla Sardo: conceptualization, formal analysis, supervision. Angiola Guidone: investigation, data curation, formal analysis, visualization. Maria Grazia Raucci: formal analysis. Anna Mariano: investigation, data curation, formal analysis. Alessandra Soriente: formal analysis. Rita Patrizia Aquino: supervision, resources. Matthew P. Wylie: writing – review & editing, resources. Giulia Auriemma: writing – review & editing, writing – original draft, supervision, resources, project administration, methodology, funding acquisition, conceptualization. Dimitrios A. Lamprou: writing – review & editing, writing – original draft, supervision, resources, project administration, methodology, funding acquisition, conceptualization.

Conflicts of interest

The authors declare that they have no known competing financial interests or personal relationships that could have appeared to influence the work reported in this paper.

Data availability

The authors declare that all data supporting the findings of this study are available within the article and its supplementary information (SI). Supplementary information is available. See DOI: https://doi.org/10.1039/d5tb01262g.

Additional supporting or minor data are available from the authors upon reasonable request.

Acknowledgements

This research was founded under the National Recovery and Resilience Plan (NRRP), Mission 4, Component 2, Investment 1.1, Call for tender No. 1409 published on 14.9.2022 by the Italian Ministry of University and Research (MUR), funded by the European Union – NextGenerationEU – Project Title P2022XZ49T – Drug eluting scaffolds for bone regeneration in osteoporosis: unveil the role of strut nanotopography and drug release pattern in the osteogenic microenvironment Acronym: OSSCA (OSteoporosis SCAffold) – CUP D53D2301871 0001-Grant Assignment Decree No. 1389 01/09/2023 adopted by the Italian Ministry of Ministry of University and Research (MUR).

References

1 G. Auriemma, C. Tommasino, G. Falcone, T. Esposito, C. Sardo and R. P. Aquino, *Molecules*, 2022, **27**, 2784.

2 M. Batista, J. Mora-Jimenez, J. Salguero and J. M. Vazquez-Martinez, *Appl. Sci.*, 2024, **14**, 3607.

3 J. Zhang, Q. Hu, S. Wang, J. Tao and M. Gou, *Int. J. Bioprint.*, 2020, 6.

4 D. Bahati, M. Bricha and K. El Mabrouk, *Adv. Eng. Mater.*, 2023, **25**, 2200859.

5 T. M. Koushik, C. M. Miller and E. Antunes, *Adv. Healthcare Mater.*, 2025, 2402953.

6 A. Bunin, O. Harari-Steinberg, D. Kam, T. Kuperman, M. Friedman-Gohas, B. Shalmon, L. Larush, S. I. Duvdevani and S. Magdassi, *Mater. Today Bio*, 2025, **30**, 101384.

7 M. A. El-Tayeb, T. M. Dawoud, K. S. Almaary, F. Ameen and H. A. Khonakdar, *J. Polym. Environ.*, 2025, **33**, 358–373.

8 W. L. Ng, J. M. Lee, M. Zhou, Y.-W. Chen, K.-X. A. Lee, W. Y. Yeong and Y.-F. Shen, *Biofabrication*, 2020, **12**, 022001.

9 C. Hart, C. M. Didier, F. Sommerhage and S. Rajaraman, *Biosensors*, 2020, **10**, 152.

10 F. Xu, H. Jin, Z. Zhou, A. Jiang, L. Liu, H. Fang, Q. Gao, Y.-C. Su, Z. Ding, Q. Chen, S. Chen and D. Sun, *J. Manuf. Process.*, 2025, **136**, 370–379.

11 N. A. Chartrain, C. B. Williams and A. R. Whittington, *Acta Biomater.*, 2018, **74**, 90–111.

12 R. Dwivedi, S. Kumar, R. Pandey, A. Mahajan, D. Nandana, D. S. Katti and D. Mehrotra, *J. Oral Biol. Craniofac. Res.*, 2020, **10**, 381–388.

13 J. Field, J. W. Haycock, F. M. Boissonade and F. Claeyssens, *Molecules*, 2021, **26**, 1199.

14 A. Ronca, S. Ronca, G. Forte and L. Ambrosio, *Methods Mol. Biol.*, 2021, **2147**, 55–62.

15 F. Wang, D. Xia, S. Wang, R. Gu, F. Yang, X. Zhao, X. Liu, Y. Zhu, H. Liu and Y. Xu, *Bioact. Mater.*, 2022, **13**, 53–63.

16 J. Wang, J. Li, X. Wang, Q. Cheng, Y. Weng and J. Ren, *React. Funct. Polym.*, 2020, **155**, 104695.

17 H. Kweon, M. K. Yoo, I. K. Park, T. H. Kim, H. C. Lee, H.-S. Lee, J.-S. Oh, T. Akaike and C.-S. Cho, *Biomaterials*, 2003, **24**, 801–808.

18 Y.-L. Cheng and F. Chen, *Mater. Sci. Eng., C*, 2017, **81**, 66–73.

19 Q. Thijssen, K. Cornelis, R. Alkaissy, J. Locs, L. V. Damme, D. Schaubroeck, R. Willaert, S. Snelling, P.-A. Mouthuy and S. Van Vlierberghe, *Biomacromolecules*, 2022, **23**, 1366–1375.

20 D. Sakarya, T. Zorlu, S. Yücel, Y. M. Sahin and A. C. Özarslan, *Polymers*, 2024, **16**, 534.

21 J. El Hayek, H. Belaid, L. C. de Saint Cyr, G. El Chawich, E. Coy, I. Iatsunskyi, C. Gervais, J. Elango, C. Zamora-Ledezma and M. Bechelany, *Mater. Adv.*, 2024, **5**, 3228–3246.

22 T. N. Palhares, J. F. P. Lovo, G. C. Rodrigues, A. L. Poli, M. A. Sabino, R. Rozental and C. C. Schmitt, *Int. J. Adv. Med. Biotechnol.*, 2024, **6**, 77–90.

23 L. Elomaa, E. Keshi, I. M. Sauer and M. Weinhart, *Mater. Sci. Eng., C*, 2020, **112**, 110958.

24 H. Nguyen, Y.-T. Chen, Y. Chen and J. Wang, *ACS Appl. Eng. Mater.*, 2023, **1**, 2723–2733.

25 R. Liang, Y. Gu, Y. Wu, V. Bunpetch and S. Zhang, *ACS Biomater. Sci. Eng.*, 2020, **7**, 806–816.

26 J. R. Coury, K. F. Skaggs, G. F. Marciano, T. Pinyavat, M. Naseef, B. D. Roye and M. G. Vitale, *JBJS Case Connect.*, 2022, **12**, e21.

27 Z. Dong, Q. Yuan, K. Huang, W. Xu, G. Liu and Z. Gu, *RSC Adv.*, 2019, **9**, 17737–17744.

28 G. Cavallaro, C. Sardo, E. F. Craparo and G. Giammona, *Molecules*, 2021, **26**, 1713.

29 C. Sardo, G. Auriemma, C. Mazzacano, C. Conte, V. Piccolo, T. Ciaglia, M. Denel-Bobrowska, A. B. Olejniczak, D. Fiore and M. C. Proto, *Pharmaceutics*, 2024, **16**, 971.

30 C. Sardo, E. F. Craparo, B. Porsio, G. Giammona and G. Cavallaro, *Biomacromolecules*, 2016, **17**, 2352–2366.

31 C. Sardo, T. Mencherini, C. Tommasino, T. Esposito, P. Russo, P. Del Gaudio and R. P. Aquino, *Drug Delivery Transl. Res.*, 2022, **12**, 1974–1990.

32 H. Bakirhan and E. Karabudak, *Int. J. Vitam. Nutr. Res.*, 2021, **1**, 85–96.

33 G. Tripodo and D. Mandracchia, *Eur. J. Pharm. Biopharm.*, 2019, **141**, 21–36.

34 R. Wang, H. Shan, G. Zhang, Q. Li, J. Wang, Q. Yan, E. Li, Y. Diao and L. Wei, *Carbohydr. Polym.*, 2022, **294**, 119742.

35 C. Yan, D. Huang, X. Shen, N. Qin, K. Jiang, D. Zhang and Q. Zhang, *Int. J. Biol. Macromol.*, 2019, **133**, 446–456.

36 G. Tripodo, G. Pitarresi, F. S. Palumbo, E. F. Craparo and G. Giammona, *Macromol. Biosci.*, 2005, **5**, 1074–1084.

37 L. Vervoort, I. Vinckier, P. Moldenaers, G. Van den Mooter, P. Augustijns and R. Kinget, *J. Pharm. Sci.*, 1999, **88**, 209–214.

38 G. Pitzanti, V. Mohylyuk, F. Corduas, N. M. Byrne, J. A. Coulter and D. A. Lamprou, *Drug Delivery Transl. Res.*, 2023, 1–14.

39 K. H. Ahmad, Z. Mohamad, Z. I. Khan and M. Habib, *Polymers*, 2025, **17**, 97.

40 H. Goodarzi Hosseinabadi, A. Biswas, A. Bhusal, A. Yousefinejad, A. Lall, W. H. Zimmermann, A. K. Miri and L. Ionov, *Small*, 2024, **20**, 2306387.

41 G. González, D. Baruffaldi, C. Martinengo, A. Angelini, A. Chiappone, I. Roppolo, C. F. Pirri and F. Frascella, *Nanomaterials*, 2020, **10**, 1788.

42 C.-A. Dantagnan, P. François, S. Le Goff, J.-P. Attal and E. Dursun, *Clin. Oral Investig.*, 2023, **27**, 2935–2942.

43 A. Baranowska-Korczyc, A. Warowicka, M. Jasiurkowska-Delaporte, B. Grześkowiak, M. Jarek, B. M. Maciejewska, J. Jurga-Stopa and S. Jurga, *RSC Adv.*, 2016, **6**, 19647–19656.

44 O. Hartman, C. Zhang, E. L. Adams, M. C. Farach-Carson, N. J. Petrelli, B. D. Chase and J. F. Rabolt, *Biomaterials*, 2010, **31**, 5700–5718.

45 A. Dedeloudi, L. Martinez-Marcos, T. Quinten, S. Andersen and D. A. Lamprou, *Expert Opin. Drug Delivery*, 2024, 1–13.

46 C. Tommasino, C. Sardo, A. Guidone, A. Soriente, M. G. Raucci, T. Ciaglia, G. Auriemma and R. P. Aquino, *J. Drug Delivery Sci. Technol.*, 2025, 106679.

47 Á. Juhász, D. Ungor, K. Berta, L. Seres and E. Csapó, *J. Mol. Liq.*, 2021, **328**, 115405.

48 L. Elomaa, S. Teixeira, R. Hakala, H. Korhonen, D. W. Grijpma and J. V. Seppälä, *Acta Biomater.*, 2011, **7**, 3850–3856.

49 H. Li, K. Yu, P. Zhang, Y. Ye and Q. Shu, *J. Biomater. Appl.*, 2022, **37**, 538–550.

50 C. A. Murphy, K. S. Lim and T. B. Woodfield, *Adv. Mater.*, 2022, **34**, 2107759.

51 B. J. Green, K. S. Worthington, J. R. Thompson, S. J. Bunn, M. Rethwisch, E. E. Kaalberg, C. Jiao, L. A. Wiley, R. F. Mullins and E. M. Stone, *Biomacromolecules*, 2018, **19**, 3682–3692.

52 D. Sakarya, F. B. Barlas, Y. M. Sahin and S. Yucel, *Main Group Chem.*, 2024, **23**, 271–282.

53 Y.-L. Cheng, Y.-K. Yang and J.-Y. Hou, Preparation and characterization of photo-curable PCL/PEG-diacrylate for additive manufacturing tissue engineering scaffold application, *Proceedings of Progress in Additive Manufacturing (Pro-AM)*, Singapore, 2014.

54 C. Curti, D. J. Kirby and C. A. Russell, *Int. J. Pharm.*, 2024, **653**, 123862.

55 X. Xu, S. Awwad, L. Diaz-Gomez, C. Alvarez-Lorenzo, S. Brocchini, S. Gaisford, A. Goyanes and A. W. Basit, *Pharmaceutics*, 2021, **13**, 1421.

56 M. Kumar, S. Ghosh, V. Kumar, V. Sharma and P. Roy, *J. Manuf. Process.*, 2022, **77**, 301–312.

57 M. Sandmeier, N. Paunovic, R. Conti, L. Hofmann, J. Wang, Z. Luo, K. Masania, N. Wu, N. Kleger and F. B. Coulter, *Macromolecules*, 2021, **54**, 7830–7839.

58 Y. Yang, Y. Zhou, X. Lin, Q. Yang and G. Yang, *Pharmaceutics*, 2020, **12**, 207.

59 N. Zirak, M. Shirinbayan, K. Benfriha, M. Deligant and A. Tcharkhtchi, *J. Appl. Polym. Sci.*, 2022, **139**, 52248.

60 P. Blyweert, V. Nicolas, V. Fierro and A. Celzard, *Ind. Crops Prod.*, 2023, **203**, 117179.

61 J. Bennett, *Addit. Manuf.*, 2017, **18**, 203–212.

62 D. Song, A. Husari, F. Kotz-Helmer, P. Tomakidi, B. E. Rapp and J. Rühe, *Small*, 2024, **20**, 2306682.

63 S. Channasanon, P. Kaewkong, S. Chantaweroad, P. Tesavibul, Y. Pratumwal, S. Otarawanna, S. Kirihara and S. Tanodekaew, *Comput. Methods Biomech. Biomed. Eng.*, 2024, **27**, 587–598.

64 M. Reymus, N. Lümkemann and B. Stawarczyk, *Int. J. Comput. Dent.*, 2019, **22**, 231–237.

65 C. Schmidleithner, S. Malferrari, R. Palgrave, D. Bomze, M. Schwentenwein and D. M. Kalaskar, *Biomed. Mater.*, 2019, **14**, 045018.

66 A. Kołodziej, E. Długoń, M. Świętek, M. Ziąbka, E. Dawiec, M. Gubernat, M. Michalec and A. Wesełucha-Birczyńska, *J. Compos. Sci.*, 2021, **5**, 20.

67 G. Kister, G. Cassanas, M. Bergounhon, D. Hoarau and M. Vert, *Polymer*, 2000, **41**, 925–932.

68 U. Murmu, J. Adhikari, A. Naskar, D. Dey, A. Roy, A. Ghosh and M. Ghosh, Mechanical Properties of Crystalline and Semicrystalline Polymer Systems, *Encyclopedia of Materials: Plastics and Polymers*, Elsevier, 2022, pp. 1–20, DOI: 10.1016/B978-0-12-820352-1.00248-0.

69 D. Lunter, V. Klang, A. Eichner, S. M. Savic, S. Savic, G. Lian and F. Erdő, *Pharmaceutics*, 2024, **16**, 817.

70 A. Frank, S. K. Rath and S. S. Venkatraman, *J. Controlled Release*, 2005, **102**, 333–344.

71 J.-C. Jeong, J. Lee and K. Cho, *J. Controlled Release*, 2003, **92**, 249–258.

72 J. Udensi, J. Loughman, E. Loskutova and H. J. Byrne, *Molecules*, 2022, **27**, 9017.

73 J. Qin, M. S. Kim, K. Chao, S. Dhakal, B.-K. Cho, S. Lohumi, C. Mo, Y. Peng and M. Huang, *Postharvest Biol. Technol.*, 2019, **149**, 101–117.

74 M. Lebedevaite, J. Ostrauskaite, E. Skliutas and M. Malinauskas, *Polymers*, 2019, **11**, 116.

75 C. Tommasino, G. Auriemma, C. Sardo, C. Alvarez-Lorenzo, E. Garofalo, S. Morello, G. Falcone and R. P. Aquino, *Int. J. Pharm.*, 2023, **641**, 123093.

76 R. M. Michell and A. J. Müller, *Prog. Polym. Sci.*, 2016, **54–55**, 183–213.

77 O. Lužanin, V. Gudurić, A. Bernhardt, D. Movrin, L. Damjanović-Vasilić, P. Terek, G. Ostojić and S. Stankovski, *Polymers*, 2023, **15**, 1468.

78 Z. Miri, H. J. Haugen, D. Loca, F. Rossi, G. Perale, A. Moghanian and Q. Ma, *J. Eur. Ceram. Soc.*, 2024, **44**, 23–42.

79 X.-Y. Zhang, G. Fang and J. Zhou, *Materials*, 2017, **10**, 50.

80 L. Rojas-Rojas, G. Tozzi and T. Guillén-Girón, *Life*, 2023, **13**, 2141.

81 S. Eshraghi and S. Das, *Acta Biomater.*, 2010, **6**, 2467–2476.

82 H. Shi, Z. Yan, J. Shi, Z. Yang, Y. Gao, J. Xu and Z. Liu, *J. Mech. Phys. Solids*, 2024, **193**, 105906.

83 K. M. N'Gatta, H. Belaid, J. El Hayek, E. F. Assanvo, M. Kajdan, N. Masquelez, D. Boa, V. Cavaillès, M. Bechelany and C. Salameh, *Sci. Rep.*, 2022, **12**, 21244.

84 J. Zhang, J. Li, G. Jia, Y. Jiang, Q. Liu, X. Yang and S. Pan, *RSC Adv.*, 2017, **7**, 56732–56742.

85 A. Wibowo, C. Vyas, G. Cooper, F. Qulub, R. Suratman, A. I. Mahyuddin, T. Dirgantara and P. Bartolo, *Materials*, 2020, **13**, 512.

86 L. Sun, J. Guo, H. Chen, D. Zhang, L. Shang, B. Zhang and Y. Zhao, *Adv. Sci.*, 2021, **8**, 2100126.

87 C. Gonçalves, J. Gomes, F. R. Maia, H. Radhouani, S. Silva, R. Reis and J. Oliveira, *Mater. Chem. Front.*, 2021, **5**, 6582–6591.

88 E. Daskalakis, M. H. Hassan, A. M. Omar, A. A. Acar, A. Fallah, G. Cooper, A. Weightman, G. Blunn, B. Koc and P. Bartolo, *Polymers*, 2023, **15**, 670.

89 N. Geoghegan, M. O'Loughlin, C. Delaney, K. D. Rochfort, M. Kennedy, S. Kolagatla, L. Podhorska, B. J. Rodriguez, L. Florea and S. M. Kelleher, *Biomater. Sci.*, 2023, **11**, 3077–3091.

90 Y. Yang, Z. Liang, R. Zhang, S. Zhou, H. Yang, Y. Chen, J. Zhang, H. Yin and D. Yu, *Polymers*, 2024, **16**, 501.

91 M. Unger, C. Vogel and H. W. Siesler, *Appl. Spectrosc.*, 2010, **64**, 805–809.

92 S. Tajvar, A. Hadjizadeh and S. S. Samandari, *Int. Biodeterior. Biodegrad.*, 2023, **180**, 105599.

93 Y. S. de Oliveira, A. C. Oliveira and A. P. Ayala, *Eur. J. Pharm. Sci.*, 2018, **114**, 146–154.

94 S. Farquharson, A. Gift, C. Shende, F. Inscore, B. Ordway, C. Farquharson and J. Murren, *Molecules*, 2008, **13**, 2608–2627.

95 F. Wei, Y. Wei, X. Yao, X. Li, Z. Wei, S. Zhang, X. Luo, Z. Guo, Q. Liu and Q. Zhu, *J. Mater. Sci.*, 2025, 1–36.

96 H. Busari, O. T. Mefford and M. A. Vaughn, *J. Mater. Chem. B*, 2025, **13**, 6456–6468.

97 Y. Yang, H. Wu, Q. Fu, X. Xie, Y. Song, M. Xu and J. Li, *Mater. Des.*, 2022, **214**, 110394.

98 ISO, 2009.